

GEOLOGIC MAP OF THE BALD HILL 7.5-MINUTE QUADRANGLE, THURSTON, PIERCE, AND LEWIS COUNTIES, WASHINGTON

by Michael Polenz, Frank R. Hladky, Anita L. Bauer, Todd R. Lau,
Jeffrey H. Tepper, Elizabeth A. Nesbitt, and Gabriel Legorreta Paulín

WASHINGTON
GEOLOGICAL SURVEY
Map Series 2023-03
December 2023

INTERNALLY REVIEWED



WASHINGTON STATE DEPARTMENT OF
NATURAL RESOURCES
WASHINGTON GEOLOGICAL SURVEY

GEOLOGIC MAP OF THE BALD HILL 7.5-MINUTE QUADRANGLE, THURSTON, PIERCE, AND LEWIS COUNTIES, WASHINGTON

by Michael Polenz, Frank R. Hladky, Anita L. Bauer, Todd R. Lau,
Jeffrey H. Tepper, Elizabeth A. Nesbitt, and Gabriel Legorreta Paulín

WASHINGTON
GEOLOGICAL SURVEY
Map Series 2023-03
December 2023

*This geologic map was funded in part by
the USGS National Cooperative Geologic
Mapping Program, award no. G22AC00364*

*This publication has been subject to an iterative technical review
process by at least one Survey geologist who is not an author.
This publication has also been subject to an iterative
review process with Survey editors and cartographers.*



WASHINGTON STATE DEPARTMENT OF
NATURAL RESOURCES
WASHINGTON GEOLOGICAL SURVEY

DISCLAIMER

Neither the State of Washington, nor any agency thereof, nor any of their employees, makes any warranty, express or implied, or assumes any legal liability or responsibility for the accuracy, completeness, or usefulness of any information, apparatus, product, or process disclosed, or represents that its use would not infringe privately owned rights. Reference herein to any specific commercial product, process, or service by trade name, trademark, manufacturer, or otherwise, does not necessarily constitute or imply its endorsement, recommendation, or favoring by the State of Washington or any agency thereof. The views and opinions of authors expressed herein do not necessarily state or reflect those of the State of Washington or any agency thereof.

INDEMNIFICATION

Research supported by the U.S. Geological Survey, National Cooperative Geologic Mapping Program, under USGS award number G22AC00364. The views and conclusions contained in this document are those of the authors and should not be interpreted as necessarily representing the official policies, either expressed or implied, of the U.S. Government.

WASHINGTON STATE DEPARTMENT OF NATURAL RESOURCES

Hilary S. Franz—*Commissioner of Public Lands*

WASHINGTON GEOLOGICAL SURVEY

Casey R. Hanell—*State Geologist*

Jessica L. Czajkowski—*Assistant State Geologist*

Ana Shafer—*Assistant State Geologist*

Washington State Department of Natural Resources Washington Geological Survey

Mailing Address:

1111 Washington St. SE

MS 47007

Olympia, WA 98504-7007

Street Address:

Natural Resources Bldg, Rm 148

1111 Washington St SE

Olympia, WA 98504

Phone: 360-902-1450

Fax: 360-902-1785

Email: geology@dnr.wa.gov

Website: www.dnr.wa.gov/geology

Publications and Maps:

[www.dnr.wa.gov/programs-and-services/geology/](http://www.dnr.wa.gov/programs-and-services/geology/publications-and-data/publications-and-maps)

[publications-and-data/publications-and-maps](http://www.dnr.wa.gov/programs-and-services/geology/publications-and-data/publications-and-maps)



Washington Geology Library Searchable Catalog:

[www.dnr.wa.gov/programs-and-services/geology/](http://www.dnr.wa.gov/programs-and-services/geology/washington-geology-library)

[washington-geology-library](http://www.dnr.wa.gov/programs-and-services/geology/washington-geology-library)

Suggested Citation: Polenz, Michael; Hladky, F. R.; Bauer, A. L.; Lau, T. R.; Tepper, J. H.; Nesbitt, E. A.; Legorreta Paulín, Gabriel, 2023, Geologic map of the Bald Hill 7.5-minute quadrangle, Thurston, Pierce, and Lewis Counties, Washington: Washington Geological Survey Map Series 2023-03, 1 sheet, scale 1:24,000, with 37 p. text. [https://www.dnr.wa.gov/publications/ger_ms2023-03_geol_map_bald_hill_24k.zip]

Cover image: Michael Polenz in front of Lahar deposits from Mount Rainier's Summerland eruptive period at age sites GD1-GD3 on the west side of the Nisqually River. See Fig. 1 for details. Photo by Trevor Contreras (WGS).



POLENZ, MICHAEL

Michael Polenz
December 2023

Contents

Introduction	1
Geologic Overview	1
Bedrock	1
Unlithified Deposits	2
Overview of Regional Structure	2
Methods	3
Geologic Mapping	3
Geophysics	3
Description of Map Units	3
Holocene to Pleistocene Nonglacial Deposits	3
Late Pleistocene Glacial and Nonglacial Sediments	6
Pliocene to Miocene(?) Sediments	10
Oligocene to Eocene Sedimentary Rocks	10
Late to Middle Eocene Volcanic and Intrusive Rocks of the Northcraft Formation	11
Discussion	14
Age of Late Holocene Sediment	14
Age of Pliocene–Miocene Sediment	15
Age of Continental to Nearshore Sedimentary Rocks	15
Age of Eocene Northcraft Formation	15
Water Quality	15
Landforms and Vashon Ice Incursion	15
Geochemistry	16
Structure and Geophysics	17
Suggestions for Further Study	19
Acknowledgments	19
Worker Contributions	19
References	19
Appendix A. Geochronology	25
Appendix B. Geochemistry	33
Appendix C. Geophysics	34
Appendix D. Landsat Spectral Image Analysis	37

FIGURES

Figure 1. Photo of lahar deposits exposed in cutbank on west side of Nisqually River	7
Figure 2. Photo of unit RMc at age site GD6	10
Figure 3. Total alkalis versus silica plot	12
Figure 4. AFM diagram	16
Figure 5. MORB-normalized spider diagram	16
Figure 6. Harker variation diagrams	17
Figure 7. Photo of a fault east of Green Hill	18

Contents (continued)

TABLES

Table 1. Summary of age analyses.....	4
Table 2. Lithologic assemblages	6
Table 3. Trends in ages and chemical traits of Northcraft Formation samples	15
Table A1. Radiocarbon results from age sites GD1–GD4	25
Table A2. $^{238}\text{U}/^{206}\text{Pb}$ ages of zircons.....	27
Table A3. New $^{40}\text{Ar}/^{39}\text{Ar}$ ages	30

MAP SHEET

Geologic map of the Bald Hill 7.5-minute quadrangle, Thurston,
Pierce, and Lewis Counties, Washington

Figure M1. Geophysical interpretation for the map area

Geologic Map of the Bald Hill 7.5-minute Quadrangle, Thurston, Pierce, and Lewis Counties, Washington

by Michael Polenz¹, Frank R. Hladky¹, Anita L. Bauer¹, Todd R. Lau¹, Jeffrey H. Tepper², Elizabeth A. Nesbitt³, and Gabriel Legorreta Paulín⁴

¹ Washington Geological Survey
1111 Washington St SE
MS 47007
Olympia, WA 98504-7007

² Department of Geology
University of Puget Sound
1500 N Warner St. #1048
Tacoma, WA 98416-1048

³ The Burke Museum of Natural
History and Culture
University of Washington
4300 15th Ave NE
Seattle, WA 98108-1446

⁴ Instituto de Geografía,
Universidad Nacional
Autónoma de México
Ciudad Universitaria
Del Coyoacán
cp 04510, México, D.F.

ABSTRACT

We present a geologic map of the Bald Hill quadrangle located along the Nisqually River in Washington's southeastern Puget Lowland. The map describes the age, stratigraphy, and distribution of glacial, fluvial, and volcanic deposits along the southern margin of the Tacoma basin. We use 38 geochemical analyses to characterize volcanic, volcanoclastic, and intermediate igneous intrusive rocks of the Eocene Northcraft Formation. The volcanic rocks are mostly andesitic but range from basalt to rhyolite. These rocks commonly include propylitic alteration, especially near intrusions. The volcanoclastic rocks range from welded to unwelded tuff, tuff breccia, and coarse, bouldery lahar deposits. Eleven new ages from the Northcraft Formation range from 42.5 ± 0.1 Ma to $<35.2 \pm 1.2$ Ma.

Our analysis of existing aeromagnetic and new gravity data suggests that the map area marks the southeastern terminus of the Olympia fault. Joint two-dimensional forward modeling of aeromagnetic and gravity data permits either a faulted or folded southern edge of the Tacoma basin. New detrital zircon ages reveal that sediment (unit **RMC**), which closely resembles the Mashel Formation in outcrop, is Pliocene—significantly younger than the fossil-based Miocene age of the Mashel Formation. Definitive determination of whether unit **RMC** is equivalent to the Mashel Formation awaits improved geochronologic age control on the Mashel Formation type section. Based on three radiocarbon dates, heavy mineral content in pumice pebbles, and geochemical analyses of three clasts, we associate lahar deposits near the northern map boundary with Mount Rainier's late Holocene Summerland eruptive period. These deposits document infrequent but life-threatening volcanic hazards. Vashon glacial deposits, Holocene alluvium, and underlying Cascade Range-derived sediment provide productive aquifers. High arsenic content in groundwater in the northeastern part of the map area may be associated with unit **RMC**.

INTRODUCTION

The map area is located 35 km southeast of Olympia and straddles the Puget Lowland and the western foothills of the Cascade Range. The map area is primarily used for forestry, rural residences, agriculture, and conservation. Quarries yield aggregate from glacial outwash and volcanic bedrock.

This map continues a campaign of 1:24,000-scale mapping that started west of the current map area (Polenz and others, 2021, 2022). It aims to provide geologic context for private and public land-use decisions and improve our understanding of geologic hazards (earthquakes, landslides, lahars, and floods) and geologic resources (water and quarry rock) in the area. The map builds upon prior mapping in and near the study area that began in the 20th century (Bretz, 1913; Mundorff and others, 1955; Snively and others, 1958; Noble and Wallace, 1966; Walters and Kimmel, 1968; Schasse, 1987; Walsh and others, 1987, 2003a; Drost and others, 1999; Polenz and others, 2021). The

map and this report provide insight into rock types, properties, and ages, and the processes that formed the landscape—from Eocene volcanism that formed the upland hills, to Pleistocene glacial scour and deposition, and post-glacial alluviation and lahar deposition. The map and report also offer an updated perspective on the gravity and magnetic anomalies at the southern edge of the Tacoma basin, and on the potential fields lineament known as the Olympia structure (Daneš and others, 1965; Odum and others, 2016), which was recently interpreted as a fault (Polenz and others, 2021, 2022).

GEOLOGIC OVERVIEW

Bedrock

The hills in the southern half of the map area mostly expose Northcraft Formation lava flows, pyroclastic and volcanoclastic

rocks, and dikes (Schasse, 1987). Compositionally, these rocks are mostly andesitic, but range from basalt to andesite (Schasse, 1987) and rhyolite (Phillips and others, 1989; Polenz and others, 2021, 2022; see *Geochemistry*). Intrusive rocks west of the map area are also Northcraft Formation, and intrusions in the Tacoma basin, inferred from geophysical data, may be similar in age (Polenz and others, 2021, 2022). Sedimentary rocks exposed in the hills south of the Deschutes River resemble those mapped as Skookumchuck and McIntosh Formations south, southwest, and west of the map area. They are all Eocene terrestrial to deltaic and marine sedimentary rocks associated with the Puget Group and interfingering with the Northcraft Formation (Snively and others, 1951, 1958, 1959; Buckovic, 1979; Schasse, 1987; Flores and Johnson, 1995; Polenz and others, 2018, 2020; Sadowski and others, 2018, 2019). Geophysical models (Finn, 1990; Polenz and others, 2021, 2022; unpublished records, Washington Geological Survey (WGS)) indicate that, aside from the Northcraft Formation, rocks in the subsurface of the map area include the early Eocene Crescent Formation basalt of the Siletzia terrane (Wells and others, 2014; Eddy and others, 2016, 2017) and ultramafic, relict mantle rocks (dense and strongly magnetic) deeper in the subsurface (Finn, 1990).

Northcraft Formation rocks in southwest Washington are part of the middle-to-upper-Eocene Puget Group (Snively and others, 1951, 1958; Gard, 1968; Buckovic, 1979; Hagen, 1987; Schasse, 1987; Walsh and others, 1987; Phillips and others, 1989). These rocks generally resemble middle Eocene to Pliocene, calc-alkaline volcanic rocks of the western Cascade Range of Oregon and California (Wood, 1960; McBirney, 1978; Blakely and Jachens, 1990; Wells, 1990; Christiansen and others, 2017), but also exhibit some systematic differences. Geomorphology and field textures indicate that the volcanic accumulations within and west of the map area include eroded remnants of strato-volcanoes, volcanic domes, spatter and cinder cones, and shield volcanoes (see also Polenz and others, 2021, 2022). Together these resemble the western Cascade Range of Oregon as described by Peck and others (1964), Hladky (1998), and Madin and others (2006). The volcanics within and west of the map area are Northcraft Formation and exhibit an apparent eastward-younging trend (Polenz and others, 2022; see *Discussion*). However, the Northcraft Formation in and near the map area lacks evidence of the systematic eastward tilting and stacking observed in the Cascade arc in Oregon (McBirney, 1978; Blakely and Jachens, 1990; Wells, 1990).

Unlithified Deposits

More than 70-m-thick, compact, pumice-rich fluvial and lacustrine sediment (unit **RMC**) on both sides of the Nisqually River resembles Mashel Formation (Noble and Wallace, 1966; Walters and Kimmel, 1968; Schasse, 1987), though further research will be required to definitively determine whether these units are correlative (see *Discussion*).

Younger alluvium and lahars (unit **Qpc**) locally overlie these deposits and likely include sediment pulses from volcanic activity and Pleistocene glaciations of Mount Rainier and surrounding areas (Crandell and Miller, 1974; Walsh and others, 2003a). These sediments are better exposed north and northwest of the map area, where age analyses suggest varied late Pleistocene

ages (Polenz and others, 2021, 2022). Near the Deschutes River west of Cross Section A–A' (Map Sheet), pre-Vashon sediment (unit **Qpu**) is at least partly sourced locally but may also include pre-Vashon Cordilleran drift.

Vashon Drift—Glacial till and outwash—covers the northern half of the map area and contains sediment derived from the Cascade Range and the Coast Mountains of British Columbia. Most of this lithologically diverse drift was moved into the map area by Cordilleran glacial ice and meltwater during the late Wisconsinan Vashon stage of the Fraser Glaciation (marine oxygen isotope stage¹ 2, MIS 2), when ice reached its southern terminus in the map area (Bretz, 1911, 1913; Noble and Wallace, 1966). Radiocarbon dates suggest that a gradual Vashon ice advance into the map area was followed by quick ice collapse, and both occurred between about 16 and 15.3 ka (Polenz and others, 2015; Haugerud, 2021).

Glacial scour and deposition from ice and meltwater formed a patchwork of geomorphic features and associated sediment that are readily apparent in lidar images. As previously noted in other areas, drumlins and flutes record southwestward ice movement (Brown and others, 1987), kettles and eskers mark where stagnant ice wasted away (Haugerud, 2009; Polenz and others, 2009), and channels and terraces document meltwater pathways (Bretz, 1913; Logan and others, 2009) and post-glacial Nisqually River incision.

Overview of Regional Structure

Aeromagnetic and gravity anomalies mark the location of the Olympia fault (Polenz and others, 2021, 2022) at the southwestern edge of the Tacoma basin. The northeast-down offset and northwesterly strike of the Olympia fault might fit a regional framework of basin-bounding, northwest-striking, dextral oblique faults and east–west-striking reverse faults in the Puget Lowland (Gower and others, 1985; Brocher and others, 2001). These faults are thought to collectively accommodate ongoing crustal shortening and plate rotation in the Cascadia forearc (Wells and McCaffrey, 2013; McCaffrey and others, 2013; Wells and others, 2014). North of the map area, the Tacoma basin reaches an estimated depth of 5–7 km (Daneš, 1985; Pratt and others, 1997; Brocher and others, 2001; Van Wagoner and others, 2002) and is bounded on its northern edge by the active Tacoma fault (Brocher and others, 2001; Nelson and others, 2008).

Yet the Olympia fault's slip history, sense of slip, and potential activity remain unclear (Sherrod, 2001; Magsino and others, 2003; Walsh and Logan, 2005; Clement and others, 2010; Odum and others, 2016; Polenz and others, 2016, 2021, 2022). Compared to structures farther north in western Washington,

¹ MIS: global marine oxygen isotope stage curve, where even-numbered stages are used as a proxy for timing and intensity of global glacial periods (Morrison, 1991; Lisiecki and Raymo, 2005). For discussion of Cordilleran ice advances into the Puget Lowland, see Booth and others (2004), Troost and Booth (2008), Polenz and others (2013, 2015), and Troost (2016). For timing of the MIS 2 ice advance into the map area at the southern limit of the Vashon glaciation, we refer to Polenz and others' (2015) fig. 3 and discussion, although the southern tip of their fig. 3 should have been extended south beyond the Deschutes River.

recorded seismicity is minimal along the Olympia fault and other faults farther south in western Washington, and no Quaternary tectonic deformation has been clearly connected to the Olympia fault. Moreover, the mostly volcanic rocks that fill the Tacoma basin northeast of the Olympia fault to <300 m below the surface are much thicker in the basin than similar rocks are southwest of the fault. A Northcraft age for these rocks (proposed by Polenz and others, 2022) would suggest that major north-down offset at the southern margin of the Tacoma basin is likewise Eocene. It remains unclear if the Olympia fault is fundamentally normal or transpressional, and if it remains active. Even less is known about the southern margin of the Tacoma basin east of the Olympia fault—a knowledge gap this study begins to address with two-dimensional forward modeling along Cross Section A–A’.

METHODS

Geologic Mapping

We identified units from field observations in the summer and fall of 2022. We collected field data and constructed preliminary field-based maps using Esri ArcMap. We refined the field mapping through:

1. Age analyses (Table 1, Appendix A, Data Supplement), including radiocarbon for post-glacial lahar deposits and pre-Vashon sediment, $^{40}\text{Ar}/^{39}\text{Ar}$ for eruptive or crystallization ages of volcanic rocks, and zircon U-Pb age analyses for zircon crystallization ages on Eocene volcanic rocks and detrital zircon maximum constraining ages for the deposition of Eocene and Pliocene sedimentary deposits.
2. Geochemical analyses (Appendix B, Data Supplement) to accurately classify igneous rocks and test their geologic unit association or identify their volcanic source.
3. Geophysical data collection and modeling (Appendix C, Data Supplement) to infer structures and subsurface distributions of rock types.
4. Spectral analysis of satellite images (Appendix D) to help identify rock types where field data are sparse.
5. Petrographic review of thin sections to identify rock types, minerals, alteration, and microscopic structures (such as fiamme that helped us determine if tuff breccia was deposited hot).
6. Analysis of mollusk fossils, plant macrofossils, and pollen to assist in paleoenvironmental interpretation and biostratigraphic age and correlation (Data Supplement).
7. Surveys of clast composition and weathering to assess sediment provenance, characterize units, and assist in determining relative ages (Data Supplement).
8. Analysis of well and boring records to assess thickness and character of subsurface deposits.
9. Consideration of geotechnical reports and prior geologic mapping and studies.
10. Inspection of aerial orthophotos (true color and infrared) to help identify wetland areas or land use that may have affected surficial deposits.
11. Geomorphic features identified from lidar to help infer associated geologic deposits. We used a lidar-based digital elevation model (DEM) with a 3-ft grid resolution (Pierce County, 2020; Washington Dept. of Natural Resources, 2021; U.S. Geological Survey, 2016; Puget Sound Regional Council, 2005; Weyerhaeuser written commun., 2022) to estimate site elevations and derive hillshade images, contours, and other elevation derivatives.

We report measurements and data using the metric system—except for elevation, which we report in feet-above-mean-sea-level (ft) to aid in comparison with topographic maps. We reference Folk (1980) for sedimentary rock classifications. We used the geologic time scale of the U.S. Geological Survey (USGS) Geologic Names Committee (2018). Where that scale lacks Epoch subdivisions, we referred to Walker and Geissman (2009).

Geophysics

We collected 347 new gravity measurements to construct a refined gravity map with particularly dense station spacing in and near the south half of the Bald Hill quadrangle. We then applied a quantitative algorithm to this gravity map to mark high-amplitude linear gradients (or ‘gravity max-spots’; Appendix C; Fig. M1A). Max-spots cluster along boundaries between rocks with contrasting densities, thereby allowing us to locate lithologic contacts and structures in the subsurface. Aeromagnetic data (Fig. M1A) are compiled from Blakely and others (1999, 2020). We also applied the max-spot algorithm in our interpretation of aeromagnetic gradients (‘aeromagnetic lineaments’, Fig. M1A). Forward-modeled isostatic gravity and aeromagnetic profiles along line X–X’ (Fig. M1B) quantitatively test subsurface interpretations developed from map-view geologic and geophysical data. Rock density and magnetic susceptibility measurements of samples from 49 outcrops within and beyond the map area, and from the E.F.E. Willhoite et al. No. 1 oil exploration well (Fig. M1A; Washington Geological Survey, 2019), helped constrain these models (Appendix C; Data Supplement; unpublished records, WGS; Contreras and others 2023). Appendix C contains details of gravity, magnetic, rock property, and modeling methods.

DESCRIPTION OF MAP UNITS

Holocene to Pleistocene Nonglacial Deposits

- af Artificial fill (Holocene)**—Cobbles, pebbles, sand, silt, clay, and boulders, all in varied amounts, engineered and non-engineered; placed to raise surfaces. Excludes small or shallow fills (usually less than 1.5 m thick) such as most deposits from road construction and residential development, and fills that are commonly transient, such as in quarries.
- Qp Peat (Holocene to late Pleistocene)**—Organic and organic-matter-rich sediment (peat, gyttja, muck, silt,

Table 1. Summary of age analyses. Additional sample information and analytical data are in the appendices and Data Supplement.

Sample	Material	Map Unit	Method ¹	Age ²	Notes
GD1	charcoal	Qvl	¹⁴ C-AMS	<2,414 ±29 ¹⁴ C yr BP	Maximum depositional age from charcoal fragment near base of National lahar sand 1.5 m below relict terrace surface. 2-sigma calibrated age (cal yr BP): 2,693–2,640 (10.9%) or 2,614–2,595 (4.7%) or 2,499–2,350 (79.8%).
GD2	charcoal	Qvl	¹⁴ C-AMS	<2,535 ±26 ¹⁴ C yr BP	Maximum depositional age from charcoal fragment (above GD1) from National lahar sand, 1.4 m below relict terrace surface. 2-sigma calibrated age (cal yr BP): 2,742–2,692 (34.9%) or 2,640–2,612 (16.1%) or 2,595–2,498 (44.4%).
GD3	charcoal	Qvl	¹⁴ C-AMS	<2,667 ±27 ¹⁴ C yr BP	Maximum depositional age from charcoal fragment from mud beneath National lahar, 4.5 m below relict terrace surface. 2-sigma calibrated age (cal yr BP): 2,848–2,810 (20.0%) or 2,794–2,742 (75.5%).
GD4	wood	Qpu	¹⁴ C-AMS	>43,500 ¹⁴ C yr BP	Wood fragment (sampled from drill core) from top of at least 2 m (7 ft) thick peat 35–37 m (115–122 ft) below surface.
GD5	wood	Qa	¹⁴ C	585 ±125 ¹⁴ C yr BP	Outer wood from cedar that grew on run-out sediment from the National lahar. Compiled from Scott and others (1995) who wrongly described site as 1.4 km upstream of Nisqually Indian Reservation; location corrected per Pat Pringle (written and oral commun., 2022–2023). Although our map still shows Qa at GD5, channel migration appears to have consumed the dated deposit of Qa and the underlying National lahar deposit (unit Qvl).
GD6	sand	RMc	detrital zircon U-Pb	<4.1 ±0.2 Ma	Maximum depositional age from youngest of 76 detrital zircons from pumiceous sand and mud about 2 m above Nisqually River.
GD7	dacite tuff	Evtn	zircon U-Pb	38 ±0.4 Ma	Zircon crystallization age computed using TuffZirc from a coherent group of 47 zircon ages from dacite tuff.
GD8	sandstone	Ens	detrital zircon U-Pb	<39.2 ±0.4 Ma	Maximum depositional age from youngest of 120 detrital zircons from sandstone (lowest lithology exposed at site) about 4 m above road.
GD9	dacite	Evdn	zircon U-Pb	40.5 ±0.5 Ma	Zircon crystallization age computed using TuffZirc from a coherent group of 38 zircon ages from dacite.
GD10	andesite tuff debris flow	Evcn	detrital zircon U-Pb	<39.2 ±0.7 Ma	Maximum depositional age from youngest of 60 detrital zircons from a debris flow deposit mostly consisting of andesite tuff breccia.
GD11	sandstone	Ens	detrital zircon U-Pb	<48 ±0.4 Ma	Maximum depositional age from youngest of 110 detrital zircons from marine sediment with shallow-subtidal marine fossils.
GD12	diorite	Eidn	zircon U-Pb	36.5 ±0.4 Ma	Zircon crystallization age computed using TuffZirc from a coherent group of 34 zircon ages from diorite.
GD13	sandstone	Ens	detrital zircon U-Pb	<35.2 ±1.2 Ma	Maximum depositional age from youngest of 96 detrital zircons from planar-bedded, micaceous sandstone and siltstone beneath basalt of unit Evbn.
GD14	basaltic andesite groundmass	Evan	⁴⁰ Ar/ ³⁹ Ar	37.4 ±0.08 Ma	Plateau age on columnar basaltic andesite groundmass dates eruption. Error is internal.
GD15	plagioclase in dacite pyroclastic ash flow tuff	Evtn	⁴⁰ Ar/ ³⁹ Ar	37.81 ±0.08 Ma	Plateau age dates plagioclase crystallization in dacite pyroclastic ash flow tuff. Error is internal.
GD16	plagioclase in andesite dike	Elin	⁴⁰ Ar/ ³⁹ Ar	38.13 ±0.09 Ma	Plateau age dates plagioclase crystallization in andesite dike that intruded volcanics; groundmass yielded inferior 38.93 ±0.09 Ma age. Error is internal.
GD17	plagioclase in basaltic andesite	Evan	⁴⁰ Ar/ ³⁹ Ar	42.51 ±0.11 Ma	Plateau age dates plagioclase crystallization in basaltic andesite; groundmass yielded inferior 32.87 ±0.15 Ma age. Error is internal.
GD18	bark	Qvl	¹⁴ C	220 ±70 ¹⁴ C yr BP	Compiled from Scott and others (1995): “Bark from silt-rich unit burying cedar forest; dates flow that killed flood-plain forest;” located “12.5 km upstream from main bridge crossing river near Yelm.” Location shown on Map Sheet is from Czajkowski (2016).

¹ Age analyses by: DirectAMS, GD1–GD3; Beta Analytic, GD4; Unknown facility, GD5 and GD18; Victor Valencia (Zirchron and Washington State University), GD6–GD13; Dan Miggins (Oregon State University), GD14–GD17.

² Error statements are 2 sigma for U/Pb and ⁴⁰Ar/³⁹Ar ages. ¹⁴C ages are conventional with one sigma errors, except for compiled ages GD5 and GD18, which have unknown error types. Maximum depositional ages from detrital samples (indicated by <) are ages implied for the reported geologic units; for raw ages, see Appendix A and Data Supplement.

clay, and sand) in flat-bottomed depressions or other poorly drained flat areas; mostly mapped where lidar reveals landforms that suggest an absence of appreciable active alluvial sedimentation and where we interpret true-color or infrared aerial photos as suggesting hydrophilic vegetation and (or) wet conditions. Thickness mostly unassessed. Unit Qp is post-glacial in age.

Qa **Alluvium (Holocene to late Pleistocene)**—Floodplain and channel sediment of mostly andesitic pebbles, cobbles, boulders, sand, silt, clay, and peat, all in varied amounts; gray to pale gray and brown to pale brown, weathers brown, orange, red, and yellow; fresh to mildly weathered, except where more weathered constituents were reworked from nearby older deposits; loose; mostly well rounded and moderately to well sorted; mostly trough cross-bedded where gravelly, except for unbedded debris flow deposits; mostly planar-bedded in sandy and silty flood plain deposits; compositionally similar to older alluvium of unit Qpc—mostly containing andesite, but also other igneous clasts from the Cascade Range, including from Mount Rainier (Table 2). Some exposures are reworked from Vashon Drift (‘Northern-sourced’ in Table 2) or Mashel Formation (Table 2). In the Deschutes River watershed, the unit is sourced from the Northcraft Formation and, less commonly, unit Ens (Table 2). In the Nisqually River valley, unit Qa locally includes debris flow diamicton, mud flow deposits, and lahar run-out deposits from Mount Rainier and vicinity (separately mapped as unit Qvl where well-exposed and extensive). Alluvial fan deposits are included in unit Qa where map scale precluded separate mapping. The fan deposits tend to be more angular, less sorted, and less consistently bedded than other deposits in units Qa and Qoa. Qa unit thickness is mostly unassessed, but exposures and relief suggest that >3 m is common, and on the Nisqually valley floor about 330 m west of Cross Section A–A’, well no. W6 suggests 11 m of unit thickness. Unit Qa forms a highly permeable, productive, usually unconfined aquifer that is sensitive to pollution and prone to drought near the surface. Unit Qa is mapped where alluvial transport appears active. Unit Qoa includes relict pre-modern, stationary alluvium and relict alluvial fans (no longer subject to increased debris flow hazards). Both units Qa and Qoa are generally post-glacial in age but may locally include alluvium of pre-Vashon age south of the ice limit. We map unit Qoav where relict terraces suggest alluvium deposited in response to down-valley ice-damming, and we tentatively suggest that it is Vashon-aged.

Qaf **Alluvial fan (Holocene to late Pleistocene)**—Pebbles, cobbles, sand, diamicton, silt, and boulders, all in varied amounts, deposited in broad fans where debris flows and floods spill from confined channels onto broader, less steep surfaces; gray to brown; loose; subangular to rounded; moderately to poorly sorted; mostly poorly bedded, but ranging from unbedded to well bedded; sourced from upslope deposits and

therefore lithologically similar to those; 1.5–6 m thick in most exposures. Unit Qaf was mostly mapped from fan-shaped landforms expressed in lidar and is mostly inferred to have been deposited by hazardous debris flows and floods. Unit Qaf is generally postglacial in age but some fans south of the ice limit may be older.

Qls

Landslide deposits (Holocene to Pleistocene)—Sand, silt, clay, pebbles, cobbles, and boulders, all in varied amounts, derived from deposits upslope; variably weathered; particles angular to rounded; mostly loose, unsorted, and jumbled, but stratified in some exposures and internally stratified and (or) compact in some landslide blocks; highly varied in thickness; mostly mapped from landforms expressed in lidar (for example, hummocky slopes, deranged and disrupted drainages, disrupted or irregular slopes, tilted benches in hillsides, and concave upper and convex lower slope forms). Similar landforms are common—but not necessarily indicative of landslides—on some slopes among Northcraft Formation volcanic rocks and in stagnant ice-related glacial deposits; we may therefore have failed to recognize some landslides and erroneously mapped some landslides where landforms suggest landslides but no slope failure occurred. Abundant landslides in deeply weathered sandstone and conglomerate (or unlithified sediment?) mapped as unit Ens along and south of the Deschutes River and in the Mashel Formation along the Nisqually River suggest that those two units may be particularly landslide-prone. Landslides triggered in other unlithified sediment along active river cutbanks are also common and can create secondary hazards by damming rivers (for instance, Pringle (1990)), but their deposits tend to be more quickly removed by the rivers. Unit Qls is generally post-glacial in age, but some landslides south of the ice limit may be older.

Qmw

Colluvium (Holocene to Pleistocene)—Loose soil, rocks, sand, silt, and clay, all in varied amounts, deposited by shallow ravel and soil creep; typically 1.5–6 m thick; locally includes small landslides and alluvial fans, but fan-shaped deposits in unit Qmw are typically steeper than those in unit Qaf, and based on lidar, tend to have less well-defined upslope feeder channels; shown where colluvium conceals the underlying geology; mostly identified from landforms, and may locally include outcrops of underlying deposits, especially where those are volcanic; not mapped where creeping, clayey soils appear to mantle otherwise undisturbed, smooth slope surfaces (that we mapped as underlying units). Unit Qmw is post-glacial in age but may locally range to pre-Vashon age south of the ice limit.

Qvl

Lahar deposits and lahar run-out deposits (Holocene to late Pleistocene)—Diamicton, sand, silt, and clay, and an inferred probable gravel facies unobserved in the map area but exposed down-valley (Polenz and others, 2022), where it consists mostly of unbedded pebbles and cobbles, with isolated boulders—some >3 m in diameter;

Table 2. Lithologic assemblages that distinguish northern-sourced drift, Cascade Range-sourced sediment, Mashel Formation, and sediment mapped as unit Ens.

Northern-sourced drift Based on Polenz and others (2022), and clast count C1 (Data Supplement) collected 1.4 km southeast of Clear Lake	Cascade Range-sourced sediment Based on Polenz and others (2022)	Mashel Formation Based on 50 clasts at base of type section 3.2 km east of map area	Pebble gravel mapped as unit Ens in this report Based on clast count C2 (Data Supplement) collected 690 m south of the Deschutes River and 2.9 km east of western map edge
Mostly Cascade Range-sourced (see column to the right), but: <ul style="list-style-type: none">• Includes varied amounts (commonly only trace quantities) of schist, gneiss, bright pink garnets, epidote, and granitic rocks that contain orthoclase• Lithologically diverse and rich in polycrystalline quartz (Walsh and Logan, 2005)• <60% intermediate to felsic volcanic rocks• >15% mafic igneous rocks (basalt and gabbro)	<ul style="list-style-type: none">• >60% intermediate to felsic volcanic rocks, mostly porphyritic andesite; less abundant dacite, felsic to intermediate intrusive rocks, and basalt• Other rock types absent or rare• Usually less basalt, sedimentary rocks, and according to Noble and Wallace (1966), less granodiorite than in northern-sourced drift• Less lithological diversity and less polycrystalline quartz than in northern-sourced assemblages of Walsh and Logan (2005)• Large quantities of hypersthene in rocks from Mount Rainier (Noble and Wallace, 1966)• A faintly lavender hue in gray sand exposures	<ul style="list-style-type: none">• 74% intermediate to felsic volcanic rocks• 12% intermediate to felsic intrusive rocks• 8% quartz• 6% metamorphic rocks	<ul style="list-style-type: none">• 72% intermediate to felsic volcanic rocks• 28% mafic igneous rocks

usually contains pumice in sand, less commonly so in other facies; clasts mostly andesite, followed by other Cascade Range lithologies (Table 2); matrix mostly sand but rich in pumice and volcanic glass fragments; pale gray to dark gray, with clasts and, less commonly, matrix variedly gray to lavender, lilac, red, or greenish gray; mildly to moderately weathered; generally loose but diamicton commonly stiff and crusty; clasts mostly rounded to well-rounded but ranging to angular; unsorted to poorly sorted in gravel, poorly to moderately sorted in sand; massive, less commonly poorly to well bedded and locally marked by oversteepened, swirl-shaped bedding; locally contains concave-up dish structures (from dewatering); observed unit thickness 1.5 to ≥4 m; well-exposed in channel cutbanks southwest of the Nisqually River at age sites GD1–3 (2 km southeast of northwestern map corner; Fig. 1).

Unit QvI consists of deposits from lahars (diamicton), lahar run-outs (diamicton, gravel, sand), and hyperconcentrated flows (mostly sand, commonly with pumice, some gravel). Observed contacts with underlying sediment are usually sharp and either conformable or unconformable.

We observed no contacts with upsection sediment but expect that units Qa or Qoa overlie it. Scattered boulders in some reaches of the Nisqually River appear to be mostly lag derived from unit QvI and pre-Vashon lahar deposits. The unit is post-glacial. Clast composition and geography indicate provenance from Mount Rainier and vicinity. The Mount Rainier-sourced National lahar was identified at age sites GD1 and GD2 (see *Discussion*; Tables 1 and A1).

Late Pleistocene Glacial and Nonglacial Sediments

VASHON DRIFT

Qgo **Uncompacted outwash, undivided (late Pleistocene)**—Pebble gravel, less commonly cobble and boulder gravel, pebbly sand, or sand, all in varied amounts; northern-sourced (Table 2); gray to pale gray, or mildly weathered to pale brown, brown, or variegated with iron stains; uncompacted and commonly cohesionless; well rounded to subrounded; moderately sorted to well sorted; in gravel facies clast supported, locally with matrix and interbeds of silt and sand; otherwise unbedded. Terrace risers suggest that unit thickness (in areas mapped as undivided unit Qgo) is commonly >6 m and may locally exceed 15 m. Unit Qgo and its subunits are found mainly between the Deschutes and Nisqually Rivers in channels that meltwater carved (mainly into Vashon moraine—unit Qgim). Unit Qgo tends to form flat to gently sloping terraces (or terrace flights) with relict channel forms that are mostly braided but range to straight. Undivided unit Qgo is mapped where observations or map scale did not permit mapping of its textural or paleoenvironmental subunits. Unit Qgo was deposited proglacially, is generally of Vashon recessional age, and stratigraphically overlies Vashon Till (including end moraines) and most ice-contact deposits. Along the southern ice margin, it may locally be coeval with nearby deposition of units Qgt, Qgic, and Qgim.

Although we did not definitively identify debris flow or flood runout deposits within unit Qgo, we infer their presence because the andesite-rich, Mount

Rainier-sourced Tanwax outburst flood flowed west across the map area and deposited diamicton west of Tenino, 29 km west of the map area (Pringle and Goldstein, 2002; Pringle and Goldstein written commun., 2018; Parker and others, 2008; figs. 5 and 6 of Polenz and others, 2018). Tanwax flood-associated (?), meltwater-shaped landforms are particularly distinct near the eastern map edge just south of the Nisqually River valley, where units Qgog and Qgimo occupy outwash surfaces that resemble Tanwax flood channels east of the map area. Other periglacial high discharge events may also have crossed the map area (Polenz and others, 2021; Troost, 2014). This strongly suggests that unit Qgo includes debris flow and flood runout deposits. Locally subdivided into:

Qgog Uncompacted outwash gravel (late Pleistocene)—Pebbles, cobbles, and boulders, all in varied amounts, commonly with sandy matrix and sand lenses or interbeds; debris flow deposits (diamicton) not definitively observed but suggested in the map area because the Tanwax flood (and perhaps other high discharge events) flowed across

the map area and deposited diamicton farther downstream (see unit Qgo); northern-sourced (Table 2); tan to gray; loose; variably sorted; mostly well rounded. Unit thickness is mostly unconstrained, but terrace risers and gravel pit depths suggest unit thicknesses of at least 1.5–10 m.

Qgof Proglacial outwash silt (late Pleistocene)—Silt, clayey silt, and fine sand; gray to brown; loose; well sorted and well rounded; unbedded to planar bedded; mostly feldspar, with lesser amounts of quartz and magnetite, which we interpret as consistent with a northern (Vashon glacial) sediment source. Landforms suggest approximately 10 m of unit thickness. Unit Qgof was observed in a single exposure between Green Hill and the Deschutes River and was mapped on surrounding and nearby bench landforms near the base of Green Hill. Similarity in inferred periglacial paleogeographic-depositional setting suggests that deposits in the geomorphically inferred unit Qoav may be similar, but a likelihood of

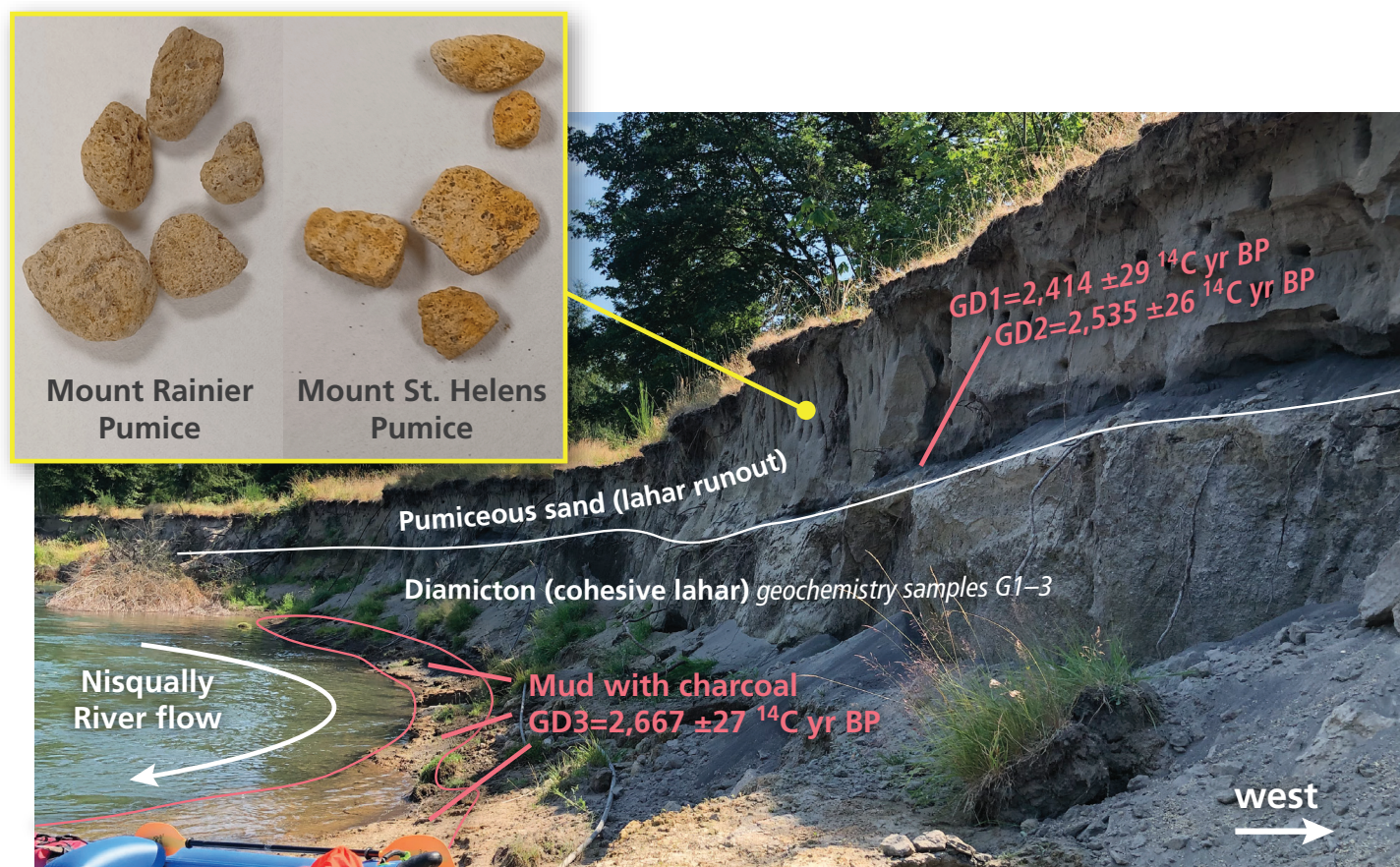


Figure 1. Lahar deposits from Mount Rainier's Summerland eruptive period exposed in a cutbank on the west side of the Nisqually River. Upper pumiceous sand layer contains a mix of <1 cm pumice clasts from the Mount Rainier C (darker, pale-brownish yellow) and the Mount St. Helens Yn (paler, orange yellow) tephra (inset, image courtesy Jim Vallance, USGS). The sand also yielded age samples GD1 and GD2 and was deposited by the non-cohesive National lahar (2,345–2,190 cal yr BP, Jim Vallance, written commun., 2022). Labeled diamicton is an earlier, cohesive lahar deposit. Radiocarbon date GD3 on detrital charcoal fragments from mud at water level suggests that all deposits are from Mount Rainier's Summerland eruptive period.

greater sediment contribution to unit Qoav from nonglacial sources to the south, and possibly coarser material, led us to separate those benches from unit Qgof.

Qgoi **Recessional ice-contact outwash, undivided (late Pleistocene)**—Cobble gravel, pebble gravel, and less commonly sand, deposited in ice-contact braid plains or channels; also sand or mixed sand and gravel in kettle walls, and sand or silt in kettle bottoms, some of which are draped with post-glacial peat where kettle bottoms are flat; tan to gray; loose; moderately to well rounded and sorted; unbedded to planar or gently cross-bedded in lake settings, and gently cross-bedded in channels or braid plains, but commonly with bedding locally oversteepened and (or) chaotic and disrupted by kettle collapse; northern-sourced (Table 2). Qgoi unit thickness is mostly unconstrained, but kettle depths, swales, and terrace risers generally suggest >3 m and at least 14 m along the western map edge north of Lackamas Creek and 20 m along the Little Deschutes River near the eastern map edge. Kettles amid unit Qgoi indicate that the unit was deposited partly on Vashon glacial ice and moraine deposits. Compared to unit Qgimo, unit Qgoi forms a more continuous, orderly drape of outwash and a generally more intact, relatively level surface with less exposure of underlying moraine.

Qgim **End moraine (late Pleistocene)**—Till, pebbles, sand, cobbles, silt, clay, and boulders, all in varied amounts; isolated lacustrine sand and silt in some kettles and peat deposits in some flat kettle bottoms; gray, tan, and reddish brown; loose to compact; unbedded in till, unbedded to bedded in other facies; northern-sourced (Table 2). Relief suggests that unit thickness commonly exceeds 20 m, except south of the Deschutes River, where it may be generally <10 m, and northeast of Elbow Lake, where it may locally exceed 75 m. Boulders (glacial erratics) commonly rest on the surface of unit Qgim. Unit Qgim and its subunit Qgimo are found mainly between the Deschutes and Nisqually Rivers, where we suspect unit Qgim also underlies much of units Qgo, Qgog, and Qgoi. Landforms within unit Qgim tend to be intensely hummocky—more than in all other units except Qls. Most of the unit is also more kettled than all other units except subunit Qgimo. Unit Qgim locally includes small, patchy terraces smoothed by meltwater and (or) draped with outwash. It also includes a few eskers. The unit undoubtedly includes some slumps, but these are mostly periglacial relicts, and unit Qgim tends to be more permeable than unit Qls, with somewhat more efficient drainage and commonly more organized drainage incision. Compared to units Qgic and Qgt, unit Qgim generally forms less streamlined surfaces with little or no evidence of drumlins and flutes. Less

compaction in most exposures additionally separates it from unit Qgt. Unit Qgim dropped out of melting, mostly stagnant ice at the southern ice margin. Unit Qgim is locally subdivided into:

Qgimo **End moraine draped with outwash (late Pleistocene)**—Glacial outwash pebbles, sand, cobbles, and boulders, all in varied amounts, resting on an end moraine consisting of till, pebbles, sand, cobbles, silt, clay, and boulders, all in varied amounts; gray, tan, and reddish brown; loose in outwash, loose to compact in moraine; moderately to well-sorted in outwash, unsorted in till; unbedded to bedded in outwash, unbedded in till. Thickness is mostly unknown, but we suspect that the surficial outwash may commonly be less than 3 m thick whereas the underlying moraine is generally much thicker, and kettle relief east of Elbow Lake locally implies >35 m total unit thickness. Like unit Qgim, the moraine deposits in unit Qgimo dropped out of melting, stagnant ice at the southern ice margin. Unit Qgimo is distinguished from unit Qgim by systematic presence in unit Qgimo of surficial outwash deposited in ice-contact channel surfaces that are now heavily fragmented by kettles. Kettles and exposures of moraine in unit Qgimo are more pervasive than those in unit Qgoi, and the outwash drape is less continuous.

Qgic **Ice contact deposits (late Pleistocene)**—Undivided till and, less commonly, outwash, consisting of loose to compact diamicton, pebble gravel (locally cobbly) and sand, all in varied amounts; northern-sourced (Table 2); pale gray to brown and reddish brown; mildly weathered except south of the Deschutes River, where weathering is varied; mostly loose and crumbly in ablation till and outwash, ranging to compact in lodgment till, but typically lacking thick, continuous, or widespread sheets of lodgment till near the surface, though small till exposures and detrital till fragments are common. Particle sizes in unit Qgic range from cobbles to medium sand, with finer particles common mainly in till matrix. Boulders are locally present in till and outwash, and loosely scattered as erratics on the surface. Rounding, sorting, and unit thickness are varied. Unit thickness is mostly unexposed, but well records and exposures in road cuts and stream cuts within and outside the map area suggest that the unit is typically 1.5–10 m thick. South of the Deschutes River the unit tends to be thinner, commonly less than 2 m thick.

North of the Deschutes River, unit Qgic is marked by irregular landforms such as kettles and sinuous channels that tend to be rounded in profile and are mostly relict (the erosional equivalent of eskers). We observed a single esker near the western map edge 4 km south of the northwestern map corner. Drumlin and flute surfaces in unit Qgic are generally more disrupted (partly by

the above-mentioned landforms) than those in unit Qgt. These landform irregularities record stagnant ice (because moving ice would smooth them out) and tend to be cored by till, sand, and gravel that is less compact, more permeable, more fragmented, more friable, and geotechnically weaker than in unit Qgt. The drumlin and flute surfaces are absent or more subdued south of the Deschutes River, where unit Qgic is also thinner and commonly contains heavily weathered matrix and clasts that could be interpreted as pre-Vashon drift. We mapped these as Vashon-aged because in our experience Vashon Drift near the ice margin commonly incorporates pre-Vashon material. Faced with few thick exposures within units Qgic and Qgt, we used landforms to help delineate unit boundaries.

Qgt Lodgment till (late Pleistocene)—Diamicton containing boulders, cobbles, pebbles, and sand, with an unsorted or poorly sorted matrix of sand- to clay-sized particles, all in varied amounts; northern-sourced (Table 2); matrix-supported in nearly all exposures; gray to pale reddish brown; mildly to moderately weathered except south of the Deschutes River, where weathering is varied; mostly compact and acting as an aquitard; not usually penetrated by roots; clasts well rounded to faceted or angular, occasionally striated; matrix mostly angular; unsorted; unbedded but in some exposures flow banded (resembling bedding); thickness mostly unexposed and likely to pinch out locally, with typically less than 3 m thickness, especially south of the Deschutes River, but well W4 north of the Deschutes River suggests more than 20 m. Unit Qgt is deposited directly by glacial ice and usually includes a loose, surficial cover of 0.5–3 m of ablation till and (or) outwash clay, silt, sand, and gravel, and scattered erratic boulders on the surface. That loose cover is the main parent material for post-glacial soil, while underlying compact lodgment till tends to be mostly unweathered. Unit Qgt tends to be more compact and resists root penetration and water percolation more effectively than unit Qgic. North of the Deschutes River, unit Qgt tends to be associated with southwest-oriented drumlins and flutes that are most strongly developed in the northeastern quarter of the map area. We attribute a paucity of drumlins and flutes south of the Deschutes River to an only brief ice advance and the shallowness of bedrock there. Unit Qgt south of the Deschutes River commonly contains heavily weathered matrix and clasts that could be interpreted as pre-Vashon drift. We mapped these as Vashon-aged because most of these exposures also include minimally weathered constituents (and not just quartz, which commonly resists weathering more than most minerals) and, in our experience, Vashon Drift near the ice margin commonly incorporates ample weathered material. Compared to unit Qgic, unit Qgt tends to form better-developed flutes and drumlins and fewer irregular surfaces (mostly meltwater channels, kettles, and eskers), and we used landforms to help delineate unit boundaries between unit Qgic and unit Qgt. Based on few, isolated exposures, unit Qgt overlies

unit Qpc (and (or) unit RMc?) north of the Deschutes River and bedrock south of the Deschutes River.

PRE-VASHON SEDIMENT

Qpc Pre-Vashon alluvium from the Cascade Range, undivided (late Pleistocene)—Pebbles, cobbles, bouldery gravel and diamicton, sand, silt, clay, and peat, all in varied amounts; Cascade Range-sourced (see Table 2 and *Late Pleistocene Glacial and Nonglacial Sediments*); pale gray to light brown, reddish brown, and pinkish brown; moderately to mildly weathered—generally more than Vashon Drift; compact; sand usually rich in plagioclase and tends to include andesitic, commonly glassy volcanic lithic fragments, with somewhat lesser amounts of quartz and (or) K-feldspar and usually distinctly less abundant opaque minerals, pyroxene, biotite, iddingsite, and other minerals. Some diamicton and boulder gravel deposits within unit Qpc appear to be lahar deposits. Unit Qpc reaches at least 50 m in thickness along the western edge of the Nisqually valley near the northwestern map corner. We also show it 5 km farther east in a small drainage (Trevor Contreras, WGS, oral commun., 2023). All other locations are queried as speculative. Unit Qpc immediately underlies Vashon till (units Qgt and Qgic). Dates from unit Qpc north and northwest of the map area suggest a patchwork of alluvium deposited by an ancestral Nisqually River during a potentially wide span of late(?) Pleistocene time (Polenz and others, 2021, 2022; Walsh and others, 2003a,b; Sisson and others, 2019).

Qpu Pre-Vashon sediment, undivided (Pleistocene)—Pebbles, cobbles, boulders, diamicton, sand, silt, clay, and peat, all in varied amounts; color and weathering varied; compact; varied grain sizes, rounding, sorting, and bedding. Unit Qpu is mapped beneath Vashon Drift (units Qgim and Qgoi) north of the Deschutes River reach west of Bald Hill, mainly based on sediment cuttings from drill hole B1 (0.34 km north of the Deschutes River). The boring intersected 26.5 m of gravel, sand, silt, and clay that we interpret as probable Vashon Drift. Below that, 8.5 m of pebble gravel, sand, and diamicton may be Vashon or older sediment. Between 35 and >37 m below the surface, the boring intersected a >2-m-thick peat deposit. A wood fragment from the top of that peat yielded a >43,500 ¹⁴C yr BP age (GD4, Tables 1 and A1), which establishes a pre-Vashon deposit. The peat rests on at least 3 m of silt and clay with wood fragments. The broader extent of unit Qpu west of B1 is suggested by another boring (not shown on map) 1 km northwest of B1, which also suggests pre-Vashon sediment beneath Vashon Drift. We separate unit Qpu from unit Qpc because Qpu may include pre-Vashon, northern-sourced glacial sediment. Its nonglacial component likely combines (1) deposits reworked from nearby and (2) sediment that an ancestral Deschutes River sourced from Northcraft Formation and unit Ens.

Pliocene to Miocene(?) Sediments

RMc **Continental sediments (Pliocene-Miocene?)**—Mostly pumiceous sand and silt with clayey matrix; commonly contains abundant pumice clasts; interbedded with thinner layers and lenses of pebble gravel with sandy to clayey matrix and mostly intermediate to felsic volcanic clasts; also tephra layers, clay, muck, peat, and plant fragments, all in varied amounts; compact and stiff but unlithified. Sand and finer sediment are pale yellow, pale gray, and white, less commonly orange, reddish brown, medium gray, and red; moderately to strongly weathered; mostly medium- to coarse-grained but ranging to very fine-grained; angular to subrounded; sorting mostly poor; most exposures distinctly trough cross-bedded or planar-bedded. Based on three thin sections, the sand composition generally is: volcanic lithic fragments (up to 60%), pumiceous glass or pumice (25–60%), quartz (10–30%), weakly pleochroic green chlorite (10–20%), plagioclase (3–15%), hornblende (trace to 10%), pyroxene (0–7%), and other opaque minerals (0–3%). Unit thickness appears to exceed 72 m in cliffs south of the Nisqually River 0.5 km west of the eastern map edge and is poorly constrained in Cross Section A–A' (see *Discussion*). Similar cliff heights suggest a similar section thickness on the north side of the valley, where trees and landslides prevent a reliable estimate. Abundant pumice clasts, fragments of glass and pumice in sand, poor sand sorting, and high angularity of sand indicate that the unit is mostly volcanoclastic. Some pumice-rich sands appear to be lahar run-out deposits. Abundant pumice clasts, lahar run-out deposits, and a

low pollen concentration but good pollen preservation at fossil site F1 (Data Supplement; Christopher Schiller, written commun., 2022; Fig. 2) together suggest that unit **RMc** may represent rapid sedimentation during a geologically brief interval. The specific volcanic source is unresolved (see *Geochemistry*). Groundwater from unit **RMc** appears prone to containing unhealthy levels of arsenic (see *Discussion*). Unit **PIMc** closely resembles the mostly sandy upper half of the Miocene Mashel Formation type section 3.2 km east of the map area (see *Discussion*). However, detrital zircon data indicate a Pliocene age for unit **PIMc** at age site GD6 ($<4.1 \pm 0.2$ Ma) (Tables 1 and A2; Fig. 2).

Oligocene to Eocene Sedimentary Rocks

ØEn **Sedimentary rocks (Oligocene-Eocene)(cross-section only)**—Fine-grained sedimentary rocks inferred upsection of unit **Evc_n** in the northern third of Cross Section A–A'. We base this inference on observations of undated fine-grained sedimentary rocks above Northcraft Formation (?) volcanoclastic rocks and lava flows in the Willhoite well 6.6 km north of the map area (Fig. M1A), and on potential fields two-dimensional forward modeling that suggests sediment or sedimentary rock with similar (low) density and magnetic susceptibility overlies unit **Evc_n** in the northern part of the map area (Figs. 1B,C). Like unit **Ens**, unit **ØEn** may include rocks of the McIntosh and Skookumchuck Formations and may interfinger with Northcraft Formation, but much or all of unit **ØEn** overlies Northcraft Formation volcanics, and unit **ØEn** may include younger sedimentary rock.

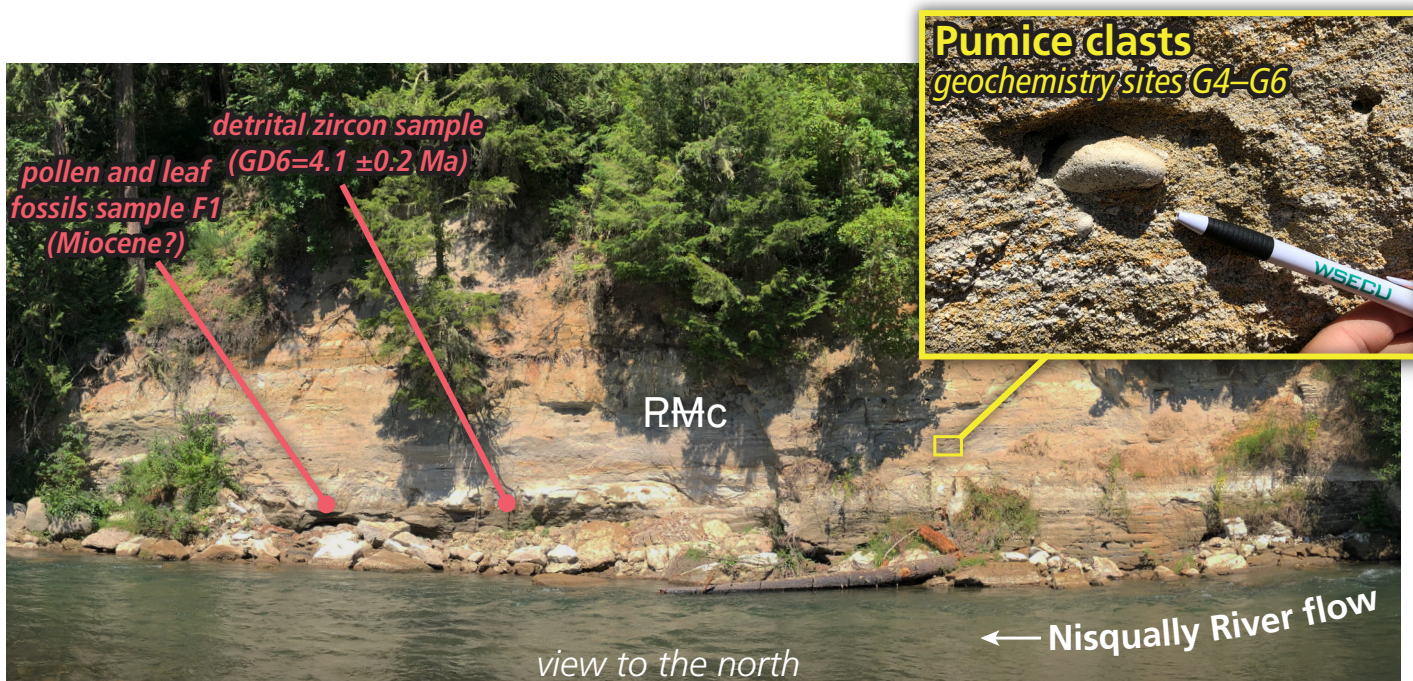


Figure 2. Unit **RMc** at age site GD6 (46.8450°N , 122.3874°W). Pumiceous sand, silt, and mud of unit **RMc** with sample sites for GD6 (detrital zircon age), pumice clast geochemistry samples G4–G6, and pollen and leaf fossil sample F1 (Data Supplement). Sediment is typical of unit **RMc** and resembles the fine-grained upper facies of the Mashel Formation type section 3.2 km east of the map area.

The approximately 150 m unit thickness suggested by Cross Section A–A' is only a very rough estimate because both the upper and lower contact elevations are poorly constrained in our modeling.

Ens **Continental to nearshore sedimentary rocks (late to middle Eocene)**—Clay-rich sandstone; brown to dark gray; fine- to very-fine-grained, moderately to well-sorted; thin-bedded and fissile; volcanic lithic.

At fossil site F4 (along Cross Section A–A') the sandstone is very-fine- to fine-grained, with ≤ 0.2 mm grains of very angular to sub-angular quartz (15–25%), altered orthoclase or sanidine (10–15%), rounded volcanic lithic fragments (15–20%), twinned broken plagioclase (1–2%), and adularia (trace), in 40–50 percent matrix of altered reddish-brown glass or clay and a few percent iron oxides. Parts of the outcrop are strongly calcareous. The site also revealed abundant marine mollusks (see *Discussion*; Data Supplement).

Geochemistry site G44 along the southern map edge is shaly, slightly micaceous, and yielded no fossils. It is 50–55 percent matrix of greenish brown to reddish brown clay minerals and reddish and black iron oxide. The 45–50 percent sand grains are angular, moderately well-sorted and 0.1–0.25 mm in size. They include quartz (35–40%), degraded volcanic lithic fragments (5–7%), plagioclase grains (3–5%), mica (2–3%), and chalcedony (trace).

Other petrographically examined samples are similarly rich in clay and volcanic lithic fragments, including some that resemble andesite of unit Eva_n . All sandstones are clay-rich and classify as graywackes. Hackly siltstone and shale are found in the unit 200–300 m north–northeast of G35 in the southern central part of the map. We suggest that the (mostly sandy) unit Ens in this map area corresponds primarily to the mostly terrestrial Skookumchuck Formation, although unit Ens may include some McIntosh Formation. We base this inference mainly on fossil content and charcoal fragments at fossil sites F2–F4 (Data Supplement), and on Polenz and others' (2020) observation that in parts of the Chehalis Basin and the Willapa Hills southwest of the map area, Skookumchuck Formation is mostly sandstone, whereas the at least partly correlative marine McIntosh Formation is mostly siltstone. Unit age may range from late to middle Eocene (see *Discussion*).

Our geophysical modeling equivalent of unit Ens (Figs. M1A, B) may range in age to early Eocene because it rests directly on Crescent Formation. At that stratigraphic level, McIntosh Formation has yielded a 47.4 ± 0.2 Ma zircon U–Pb age 35 km west of the map area (Polenz and others, 2017, 2020). Furthermore, like the “lower McIntosh” of Pease and Hoover (1957), it may interfinger with (otherwise underlying) Crescent Formation.

Late to Middle Eocene Volcanic and Intrusive Rocks of the Northcraft Formation (Puget Group)

Ev_n **Undivided igneous rocks (late to middle Eocene)**—Dark gray to medium gray lava flows, mostly andesite and basaltic andesite, but ranging from basalt to rhyolite (Fig. 3); interbedded with pale brown to brown, tan, and olive lahar deposits, pyroclastic tuff, flow breccia, and other volcanoclastic rocks; locally intruded and hydrothermally altered by chemically similar dikes, sills, and stocks. Undivided unit Ev_n is mapped where subunits could not be separated. Its age range spans at least ~7 million years, from 42.51 ± 0.11 Ma at $^{40}\text{Ar}/^{39}\text{Ar}$ age GD17 (and perhaps older where undated) to $<35.2 \pm 1.2$ Ma at detrital zircon U–Pb age GD13, based on new ages from eight samples of the Northcraft Formation subunits and interbedded sedimentary rocks (see also *Discussion*; Table 1, Appendix A, and Data Supplement). Locally subdivided into:

Ev_b_n **Basalt flows (late to middle Eocene)**—Basalt lava; medium- to light-gray, weathers brown to yellow; porphyritic. Unit Ev_{b_n} consists of 20–25 percent subhedral plagioclase phenocrysts that range from groundmass-sized microlites up to 2 mm crystals, in 75–80 percent altered greenish gray glass with up to 15 percent opaque minerals and up to 10 percent chalcedony-filled ovoid vesicles. Unit Ev_{b_n} was observed only near the southwestern map corner at and west of geochemistry site G44 at relatively high elevations (above 1,800 ft), where it overlies planar-laminated, fissile, very fine- to fine-grained sandstone (that may range to shale) of unit Ens . Our single geochemistry sample (G44; Data Supplement) displayed very high loss on ignition (11%) and petrographic evidence of alteration (groundmass chloritization, alteration of feldspars, chalcedonic alteration). Its chemical composition (Fig. 3) is close to basaltic andesite. Its alteration far exceeds that of most other lava flows sampled and is consistent with (syndepositional?) water interaction. Where observed in the map area, unit Ev_{b_n} overlies unit Ens which produced a detrital zircon U–Pb age of $<35.2 \pm 1.2$ Ma (age site GD13)—the youngest known bedrock age in the map area (Tables 1 and A2).

Ev_a_n **Andesite and basaltic andesite flows (late to middle Eocene)**—Lava flows of mainly andesite, basaltic andesite, and less commonly trachyandesite and basaltic trachyandesite (see *Geochemistry*); locally includes minor, interbedded volcanoclastic rocks; medium-dark to dark gray to dark olive gray; dense where unweathered; porphyritic with plagioclase phenocrysts up to 4 mm in length except

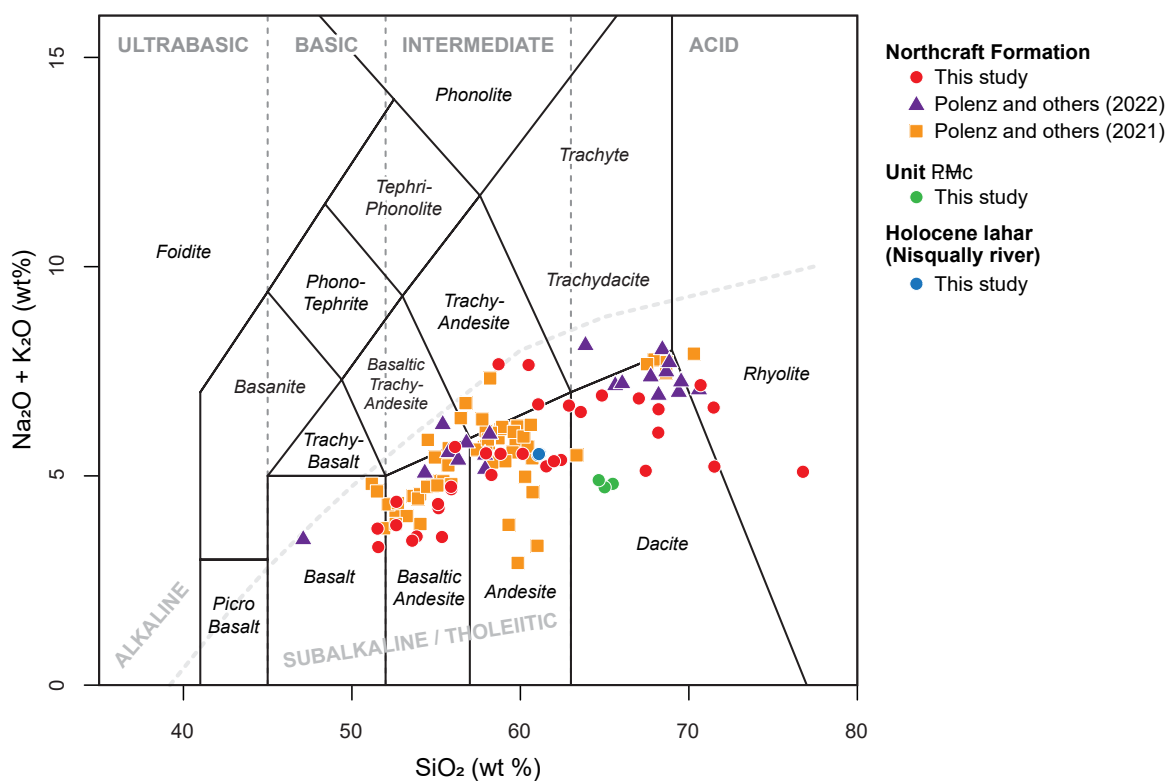


Figure 3. Total alkalis versus silica plot (Le Bas and others, 1986) with Northcraft Formation data from this study, Polenz and others (2021), and Polenz and others (2022). Note that the Bald Hill samples lack the ~61–67 wt. % SiO_2 'Daly gap' seen in data from earlier studies. Also plotted are new analyses of clasts from unit RMc and a Holocene Nisqually River lahar deposit.

where locally aphanitic; blocky. Groundmass textures range from hyalopilitic to trachytic with the basaltic andesite lava flows usually being more trachytic than either andesite or dacite. Unit Eva_n is so widely exposed that we mapped other Northcraft Formation units only where we had specific reason to think that andesite flows are not the main Northcraft Formation constituent. Intrusion of unit Eid_n at the southeastern map corner appears to have led to hydrothermal phyllic alteration (silicification, chloritization, and slight pyritization) of unit Eva_n in that area. Geochemistry sample G39 exemplifies these alteration qualities but nominally tested as basalt at 51.5 percent silica (see *Geochemistry*)—and therefore is, despite its silicification, paradoxically among the most mafic rocks observed in the map area. Two new $^{40}\text{Ar}/^{39}\text{Ar}$ ages from andesite lava flows in unit Eva_n are 42.51 ± 0.11 Ma near the western map edge (GD17) and 37.40 ± 0.08 Ma from a quarry north of Bald Hill, in the central eastern part of the map (GD14) (Tables 1 and A3).

EvCn Volcaniclastic deposits (late to middle Eocene)—Basaltic-andesitic to andesitic volcaniclastic deposits in which weathering ranges from fresh in some outcrops to highly varied elsewhere; includes:

- (1) Lithic vitric pyroclastic flow deposits; mostly multi-colored, brown, tan, pink, and olive; mostly angular to subangular blocks 0.1 m in diameter or smaller; moderately to poorly sorted; massive to thick-bedded; mostly matrix supported; mostly welded; devitrified; ranging from block and ash to lapilli-ash to ash tuff. Andesite tuff geochemistry sample G32 has 75 percent glass and includes carbonized and agatized wood (tree limb and twigs) and 3–5 percent preserved fiamme (flattened, fibrous, isotropic glass shards). Basaltic andesite tuff geochemistry samples (G12, G15, G22, and G24) are more crystal-rich and yield <50 percent glass.
- (2) Massive boulder diamict with varied amounts of matrix and welding; sub-rounded to subangular; in one exposure about 130 m south–southwest of Fossil Rock forms conglomerate in several fining-upward, mud matrix-supported, graded beds with sub-rounded to angular clasts.
- (3) Volcanic-lithic sandstone, clay-rich to clay-free, planar and graded, with centimeter- to decimeter-thick beds, moderately sorted, immature, and in

some exposures tuffaceous with minor angular lapilli and devitrified ash.

- (4) Sandy, subrounded- to rounded-pebble conglomerate.
- (5) Rare, few-meter-wide channel fills of coarse, granular, and poorly sorted sandstone.
- (6) Other isolated features including tuff breccias, gradationally bedded clastic sediments, scour surfaces, and paleosols.

Unit Evc_n forms 30–50-m-high cliffs and low prominences on the north side of Bald Hill and dip-slopes in thick-bedded deposits on its western and southwestern flanks. On Green Hill the unit forms dip-slopes of tuff and thin interbedded lava flows. Unit Evc_n is clay-rich and has low permeability. This may explain why south-facing dip-slopes in the unit seem to support only grasses, small shrubs, and sporadic trees. The unit is thickest at Bald Hill, reaching at least 400 m. The unit is well exposed in a particularly coarse, matrix-supported boulder diamictite at Deschutes Falls, where ⁴⁰Ar/³⁹Ar age sample GD16 (unit Eii_n) constrains the age of unit Evc_n to $<38.13 \pm 0.09$ Ma (Tables 1 and A3). Detrital zircons from an ash-flow tuff yielded a $<39.2 \pm 0.7$ Ma maximum constraining age at age site GD10 (Tables 1 and A2).

Evt_n Felsic tuff (late to middle Eocene)—Vitric ash flow tuff, crystal vitric ash flow tuff, and lithic lapilli-ash flow tuff; pale yellow to tan to medium light gray; dacitic (geochemistry sites G19, G21, G30; Data Supplement). West of Green Hill, the unit is unbedded and often crystal deficient. Seventy-five percent or more is altered glass (with some fiamme). The unit locally contains pumice, both as lapilli and as rare small blocks.

East and north of Green Hill the unit contains up to 5 percent hornblende, with crystals up to 3 mm in length, up to 15 percent plagioclase, with crystals up to 4 mm in length, and pumice as fiamme. Geochemistry site G21 (Data Supplement) is notably lithic and contains up to 10-cm-thick blocks of light gray felsic lava, red scoria, and yellowish tan pumice.

Near the western map edge, exposures of unit Evt_n are less crystalline, usually more altered, and often commingled with blocky dacite lava, although the boundaries are gradational to indistinct due to alteration and concealing vegetation and soil. At geochemistry site G28 near the western map edge, petrographically confirmed fiamme

bent around phenocrysts indicate welding, and altered feldspar and irregular epidote infiltration indicate hydrothermal alteration; 30–40 percent of the rock is altered plagioclase phenocrysts <2 mm in length, a third of which are anhedral and have rounded boundaries that indicate abrasive transport. Glomerocrystic epidote crystals 1–5 mm in size form 2–5 percent of the rock (some crystals are <0.1 mm in size); 5–10 percent of the rock is brownish to olive green, non-pleochroic, devitrified, and chloritized glass in sub-parallel veinlets; and 50–60 percent is cryptofelsite as mostly feldspar and a few percent chalcedony.

The maximum unit thickness we observed is about 30 m. We obtained two ages from unit Evt_n: 38.0 ± 0.4 Ma from a crystal vitric tuff at U-Pb age site GD7 and 37.81 ± 0.08 Ma from a lithic lapilli ash tuff at ⁴⁰Ar/³⁹Ar age site GD15 (Tables 1, A2, A3).

Evd_n Dacite and minor rhyolite (late to middle Eocene)—Felsic lava flows of mainly dacite but ranging to rhyolite (geochemistry sites G27, G29, G33–G35, and G37; Data Supplement); yellowish tan to brown to medium dark olive gray; blocky to massive; sparsely porphyritic. Thin sections reveal 3–5 percent slightly sericitized and chloritized plagioclase phenocrysts up to 3 mm long in an intersertal to hyalopilitic (trachytic in some samples) groundmass of variously dominant olive green glass and plagioclase microlites with 7–15 percent chlorite, opaques, and quartz. Rhyolite is mostly (95%) devitrified glass. Unit Evd_n includes some intercalated zones of felsic tuff (too small to separately map as unit Evt_n). We obtained a 40.5 ± 0.5 Ma zircon crystallization age at U-Pb age site GD9 3.4 km northeast of the southwestern map corner (Tables 1 and A2).

Evvn Vent deposits (late to middle Eocene)—Red to pink, very finely abrasive, vesicular scoria and spatter agglutinate, and dark gray, angular-block tuff breccia mixed with gray spatter; andesite composition based on a single sample (geochemistry sample G18; see *Geochemistry*; Data Supplement). Scoria is hyalopilitic, with 7–10 percent sub-ovoid to irregular vesicles <0.4 mm in diameter, 65–75 percent red glass and black oxides enveloping microlites of trace clinopyroxene, and 15–25 percent plagioclase. Tuff breccias contain porphyritic lava blocks.

Eii_n Dikes and shallow intrusions of andesite and basaltic andesite (late to middle Eocene)—Dikes and small intrusions of intermediate composition (geochemistry sites G23 at the western map edge and G16 at Deschutes Falls;

Data Supplement). Two distinct geometries are mapped: (1) tabular ‘cordwood’ dikes (wherein distinctive jointing gives appearance of stacks of split firewood) up to 3 m wide, both as single and multiple sheets of aphanitic to slightly porphyritic, medium- to dark-gray andesite, and (2) small, irregularly and lobate-shaped stocks of granular, salt-and-pepper, olive gray massive to blocky basaltic andesite found intruding both volcanoclastic and lava flow units. Andesite dikes are aphanitic to slightly porphyritic, the main phenocrysts (3–5%) being plagioclase up to 3 mm long with trace amounts to 1 percent smaller pyroxene, and 1–2 percent open vugs. Speckled olive green and black granular basaltic andesite intrusions on the west edge of the map are rich (70–80%) in very fine (≤ 0.3 mm) plagioclase crystals that often display Carlsbad twinning and always show multiple internal pockets of irregularly-zoned extinction. About 3–5 percent plagioclase phenocrysts up to 3 mm in size, however, are normally twinned and normally zoned. Interstitial dark chloritized glass and a few percent dark microcrysts of pyroxene and hornblende give the rock its speckled appearance. An andesite dike that buttresses the Deschutes Falls waterfall yielded a 38.13 ± 0.09 Ma $^{40}\text{Ar}/^{39}\text{Ar}$ age (at age site GD16) (Tables 1 and A3)—well within the range of other Northcraft Formation ages and therefore consistent with including andesitic dikes in the map area in the Northcraft Formation.

Eid_n

Diorite (late to middle Eocene)—Diorite, pale tan to pinkish gray, or speckled dark gray and pale gray; massive; finely to coarsely-crystalline (≤ 0.5 mm) with hypidiomorphic granular texture; locally contains ovoid mafic enclaves of hornblende diorite amid massive, lighter-colored plagioclase-rich diorite host that commonly forms pale, smooth, centimeter-scale veinlets that cut the dark enclaves. Petrography shows that the enclaves are enriched in hornblende and depleted in plagioclase compared to the surrounding rock. Light-colored, finely crystalline host rock (geochemistry site G40; Data Supplement) is 15–20 percent hornblende up to 0.7 mm in length; 75–80 percent plagioclase 0.2–0.7 mm in size; 1–2 percent opaques (magnetite?) ≤ 0.2 mm in size; 5–7 percent pleochroic olive green chlorite 0.07–0.3 mm in size; and 1 percent quartz ≤ 0.5 mm in size. Mafic enclaves have more hornblende and less plagioclase: 15–25 percent hornblende 0.07–0.7 mm in size; 60–65 percent plagioclase 0.2–2 mm in size; 5–10 percent chlorite 0.07–0.3 mm in size; 1–2 percent quartz up to 0.5 mm in size; and

2–3 percent magnetite 0.02–0.2 mm in size. Speckled diorite at geochemistry site G42 (Data Supplement) is 75–80 percent coarse plagioclase < 1 to 5 mm in size; 10–15 percent chlorite ≤ 1 mm in size, interstitial to plagioclase; 2–3 percent unaltered hornblende ≤ 0.7 mm in size; trace to 1 percent chlorite pseudomorphs of hornblende; trace to 1 percent quartz ≤ 0.07 mm in size, as irregular to sub-spherical blebs and interstitial fills; and trace to 1 percent pyroxene that is glomerocrystic (with itself or other mafics) up to 3 mm in size, some with ophitic intergrowths of plagioclase. In the enclaves, which show no penetrative veinlets, the plagioclase displays sericitization and the hornblende is chloritized—evidence for internal hydrothermal effects. Unit geochemistry ranges from basaltic andesite to andesite (geochemistry sites G40, G42; Data Supplement) with the andesite being richer in chlorite. Age site GD12 yielded a 36.5 ± 0.4 Ma zircon U-Pb age (Tables 1 and A2)—the youngest Northcraft Formation crystallization age in the map area.

DISCUSSION

Age of Late Holocene Sediment

At age sites GD1–GD3, a 4-m-thick exposure of unit QVl includes deposits from at least two lahars of Mount Rainier’s Summerland eruptive period, which entered the Nisqually River ~2,600–2,000 cal yr BP (Vallance and Sisson, 2022; James Vallance, U.S. Geological Survey, written commun., 2022). The upper 1–2 m of the exposure is a massive to well-bedded sand with prominent pumice fragments < 1 cm in size and also yielded charcoal fragments for age sites GDs 1–2 (Fig. 1). The pumice fragments include Mount Rainier tephra C (darker) and Mount St. Helens tephra Yn (paler), which James Vallance (U.S. Geological Survey, written commun., 2022) identified from “a heavy mineral assemblage of cumingtonite and hornblende, plus tiny magnetites” in St. Helens Yn tephra, and “augite, lesser amounts of hypersthene, and small proportions of hornblende and olivine, plus tiny magnetites” in the 2,345–2,190 cal yr BP Mount Rainier C tephra. Based on these tephra identifications and two new ^{14}C ages (age sites GD1 and GD2), we agree with Vallance (written commun., 2022) and Pat Pringle (oral commun. 2022) that the upper sand at this location is from the National lahar (Scott and others, 1995), which was triggered by explosive eruption of the C tephra during Mount Rainier’s Summerland eruptive period (Vallance and Sisson, 2022). A directly underlying 1–1.5-m-thick diamicton may be from a slightly older lahar. Scoria clasts from this diamicton (geochemistry samples G1–G3) support correlation to the Summerland eruptive period (see *Geochemistry*). This is consistent with the age of sample GD3 (2,848–2,810 or 2,794–2,742 cal yr BP) from an underlying mud layer with abundant charcoal fragments at Nisqually River level (base of exposure).

Table 3. Comparison of average radiometric ages and select chemical traits of Northcraft Formation samples from the map area and adjacent quadrangles farther west (Polenz and others, 2021, 2022). Reported uncertainties are one standard deviation. Age computations include only direct age estimates for volcanic rocks (and exclude age constraints from sedimentary rocks).

	Tenalquot Prairie / Vail	McKenna / Lake Lawrence	Bald Hill
# of dated samples	7	6	7
Mean age (Ma)	43.13 ±2.19	41.93 ±1.09	38.69 ±2.00
Mean TiO ₂ (wt. %)	1.53 ±0.37	1.10 ±0.39	1.01 ±0.27
Mean Sr/Y	14.7 ±7.5	13.5 ±7.9	21.9 ±13.3
Mean Yb (ppm)	2.8 ±0.7	2.8 ±0.8	2.2 ±0.7

Age of Pliocene–Miocene Sediment

Unit **RMc** yielded a $<4.1 \pm 0.2$ Ma age (age site GD6) 3 m above river level—near the base of the unit’s exposed section. The mostly sandy to silty unit closely resembles and appears to be stratigraphically equivalent to the upper, fine-grained facies of the Mashel Formation type section 3.2 km east of the map area—which Walters (1965) defined as Miocene based on plant macrofossils. Plant macrofossils at age site GD6 have not been assessed. Pollen at fossil site F1, collocated with age site GD6, revealed a plant community that would have been interpreted as Miocene if not for our Pliocene detrital zircon age (Christopher Schiller, written commun., 2022–2023; Data Supplement). Without either chronometric age control at the Mashel Formation type section or assessment of plant macrofossils at fossil site F1, we can neither demonstrate nor exclude that unit **RMc** at age site GD6 (fossil site F1) is Mashel Formation. Therefore, all exposures of unit **RMc** may be Mashel Formation, but we map the more general unit **RMc** because our Pliocene age at GD6 is incompatible with the plant macrofossil-based Miocene age of the Mashel Formation, and because unit **RMc** in Cross Section A–A’ may include younger and older deposits.

Age of Continental to Nearshore Sedimentary Rocks

Unit **Ens** yielded ages between $<39.2 \pm 0.4$ Ma at age site GD8 in the southern center of the map (among the lowest exposures of the unit) and $<35.2 \pm 1.2$ Ma at age site GD13 along the southern map edge (among the highest exposures in the map) (Tables 1 and A2). Marine sandstone at age site GD11 along Cross Section A–A’ yielded a $<48.0 \pm 0.4$ Ma age but was probably deposited closer to ~39 Ma because: (1) it was invaded by a tuffaceous debris flow that entrained chunks of the host sandstone and yielded a $<39.2 \pm 0.7$ Ma age (age site GD10). The flow probably would not have invaded and entrained bits of the host rock if that had already been ~9 million years old (and likely indurated); (2) elevations suggest that age site GD11 should be younger than the apparently stratigraphically lower site GD8 which yielded an age of $<39.2 \pm 0.4$ Ma; and (3) the marine fossil assemblage at age site GD11 (fossil site F4, Data Supplement) resembles that of the Cowlitz Formation type area at Olequah Creek, where tuff yielded a 39.53 ± 0.10 Ma age².

² Paul Renne, Berkeley Geochronology Center, written commun. to E. Nesbitt, 2023: age is recalibrated from 38.9 ± 0.1 Ma age reported by Irving and others (1996).

Age of Eocene Northcraft Formation

Eight new Northcraft Formation ages range from 42.51 ± 0.11 Ma (age site GD17) to 36.5 ± 0.4 Ma (age site GD12) (Tables 1, A2, A3). A maximum depositional age from unit **Ens** (GD13) beneath Northcraft Formation basalt (unit **Evn**) along the southern map edge extends the young end of the formation to $<35.2 \pm 1.2$ Ma (Tables 1 and A2). The resulting age range (42.5 Ma to <35.2 Ma) is well within the 45.80 ± 0.07 Ma to 32.7 ± 1.5 Ma range of Northcraft Formation ages reported elsewhere (Polenz and others, 2021; Hagen, 1987); a 23.2 ± 1.7 Ma age that Hagen (1987) also reported as Northcraft Formation is suspect according to Phillips and others (1986). However, ages from the map area are on average younger than those from nearby areas farther west (Table 3).

Water Quality

Elevated arsenic levels in water from some wells in the northeastern part of the map area pose a potential health concern (Tacoma-Pierce County Health Department, 2023). Naturally occurring, elevated arsenic levels in groundwater typically involve a combination of acidic groundwater and high levels of organic matter in the aquifer host sediment leading to oxidized soil organic matter and arsenic release from iron oxides (San Juan, 2022). Based on our observations, unit **RMc** typically contains more organic matter than other common aquifers, such as glacial sediment or unit **Qpc**. Compared to those units, unit **RMc** may also exhibit greater groundwater residence time (conducive to more arsenic uptake) because it likely has lower permeability, due to greater compaction and abundant clayey lacustrine and weathered volcanogenic sediments. Elevated organic content is also found in some sedimentary rocks of unit **Ens** (which includes Skookumchuck Formation), but due to their lithification and the availability of shallower aquifers in overlying sediments, the sedimentary rocks of unit **Ens** are less likely to be tapped as groundwater sources. Although we are rarely confident that well records permit us to accurately separate units **Ens**, **RMc**, **Qpc**, and glacial sediments, we suspect for the above reasons that unit **RMc** is especially prone to leaching arsenic into groundwater. The common occurrence of high arsenic levels in groundwater in the northeast part of the map area therefore suggests that the unit is widespread there.

Landforms and Vashon Ice Incursion

Landforms in the glaciated part of the map area correlate to specific map units and suggest that Vashon ice briefly advanced

to the ice limit before stabilizing at the Deschutes River. South of the Deschutes River, units Qgt and Qgc are thin, tend to contain heavily weathered material, and mostly lack glaciation-associated landforms (flutes, drumlins, eskers, kettles, and outwash channels). Their absence suggests that near the ice limit, bedrock is shallow (as locally observed), the ice was thin, and the ice incursion short-lived.

Between the Nisqually and Deschutes River valleys, greater thickness and lesser weathering of the glacial sediment suggests a longer-lasting ice front—and possibly that the drift here fills a pre-glacial trough. A thick moraine (unit Qgim) forms chaotically bumpy and kettled surfaces. Much of this moraine is draped by outwash (unit Qgimo) that formed smooth surfaces before kettles collapsed. Less interrupted, flat to gently sloping surfaces—commonly stepped in terrace flights and (or) with relict channel forms—mark other glacial outwash deposits (unit Qgo and its subunits).

Northeast of the Nisqually River, lodgment till (unit Qgt) is associated with southwest-trending drumlins and flutes smoothed by southwest-moving ice. Drumlins and flutes also record ice movement in parts of unit Qgc, but the more disrupted surfaces that generally mark unit Qgc north of the Deschutes River (see unit description) imply stagnant ice depositing melt-out till and meltwater scouring subglacial landforms and depositing sediment beneath, in, or on ice and proglacially as outwash. Therefore, unit Qgc documents areas in which ice movement had stalled near the end of the glacial incursion.

Geochemistry

Whole rock chemical analyses were determined on 44 igneous samples (Data Supplement), including 38 Northcraft Formation bedrock samples (geochemistry samples G7–G44), three pumiceous clasts from unit RMc (geochemistry samples G4–G6), and three tephra clasts from unit QvI (geochemistry samples G1–G3).

The Northcraft Formation samples span a continuum from basalt to rhyolite (51.5–76.8 wt. % SiO_2 ; 7.80–0.28 wt. % MgO) and classify as subalkaline (Fig. 3) and calc-alkaline (Fig. 4). They are moderately light rare earth element (LREE) enriched (average $\text{La}/\text{Ybn} = 7.1$) and have high field strength element (HFSE) (Ta, Nb) depletions on a MORB-normalized spider diagram (Fig. 5). These traits are all characteristic of subduction-related magmas and consistent with interpreting the Northcraft Formation as an early expression of the Cascade arc (Phillips and others, 1989; Polenz and others, 2021). For many elements these samples overlap in composition with Northcraft Formation analyses from west of the map area (Polenz and others, 2021, 2022) (Fig. 3), but there are also subtle differences: at equivalent silica content, the Bald Hill samples tend to have lower Fe_2O_3 , TiO_2 , and P_2O_5 , and higher Al_2O_3 (Fig. 6, Table 3). Among trace elements, the Bald Hill samples tend to have lower concentrations of HFSE (Zr, Nb, Ta, Nb, Hf) and REE (for instance, La, Yb), but higher Sr and Sr/Y (Fig. 6, Table 3). Lower TiO_2 , P_2O_5 , HFSE, and REE all suggest Bald Hill quadrangle magmas came from a more depleted mantle source, whereas higher Sr and Sr/Y and lower Yb indicate residual garnet in the source, which implies melting and (or) melt evolution at greater depth (>30 km), below the stability limit of plagioclase.

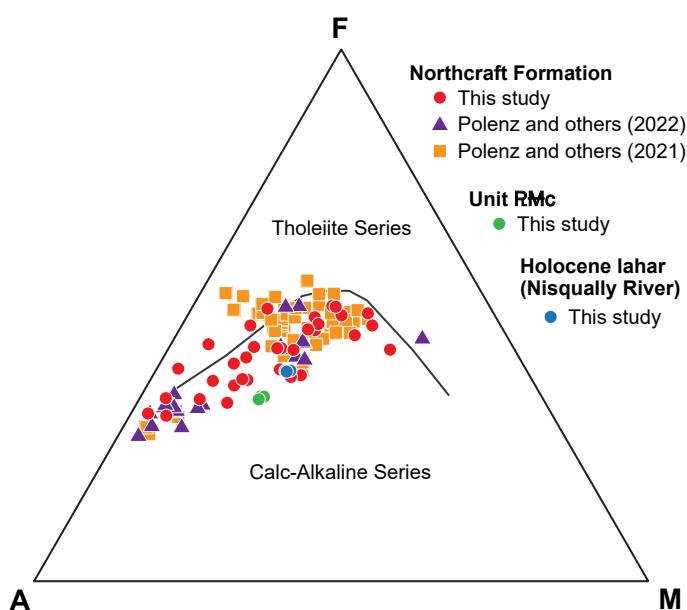


Figure 4. Alkali, iron, and magnesium (AFM) ternary plot (Irvine and Baragar, 1971) showing that most Northcraft Formation samples as well as the Mashel Formation and lahar clast samples classify as calc-alkaline. Symbols are the same as in Figure 3.

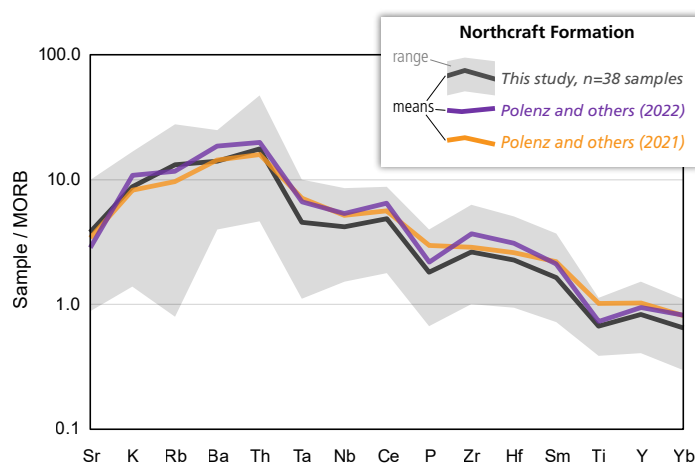


Figure 5. MORB-normalized spider diagram showing K-Rb-Ba-Th enrichments and Ta-Nb depletions characteristic of subduction-related magmas. Shaded region outlines the range for the 38 Northcraft Formation samples analyzed in this study. Lines are averages for this study, Polenz and others (2021), and Polenz and others (2022). Depletions in P and Ti reflect fractionation of apatite and ilmenite in some samples. Data normalized to the MORB values of Sun and McDonough (1989).

Radiometric ages indicate that Northcraft Formation magmatism in and near the map area may have migrated eastward over time (Table 3). Thus the chemical differences may reflect spatial shifts (for instance, heterogeneous mantle wedge) or temporal changes (such as progressive depletion of the mantle and (or) thickening of the crust as the arc matured).

Three pumiceous clasts from unit RMc (geochemistry samples G4–6, Fig. 2) are calc-alkaline dacites of nearly identical composition (64.6–65.4 wt. % SiO_2 , 2.05–2.10 wt. % MgO) (Figs. 3 and 4). All have adakite traits, including $\text{Sr} > 400$ ppm, $\text{Sr}/\text{Y} > 20$, $\text{Yb} < 1.8$ ppm, and high La/Ybn (average = 12.7). Based on these traits and maximum constraining age GD6 ($< 4.1 \pm 0.2$ Ma)

these clasts were sourced from the Cascade Range but do not match a specific, known volcanic center.

The lahar clasts from unit QvI (geochemistry samples G1–3, Fig. 1) classify as calc-alkaline andesites (61.0–61.2 wt. % SiO₂, 3.13–2.98 wt. % MgO) (Figs. 3 and 4), very uniform in composition and likely from a single eruption. They are distinguished by high Sr (586–604 ppm) and other adakite characteristics (for instance, Sr/Y = 62–68, Yb = 1.6–1.7 ppm), which are also characteristic of andesitic pumice and lavas from the Summerland eruptive period at Mount Rainier (Sisson and Vallance, 2009). Based on the close similarities in composition and age, geochemistry samples G1–3 appear to be associated with that episode (see also *Age of Late Holocene Sediment*).

Structure and Geophysics

BEDDING ORIENTATIONS

Bedrock

Despite relatively few recorded orientations, our field work produced a strong sense that structural dips are generally gentle and some deposits were not originally horizontal. Examples are 7 to >15 degree dips observed among tuff breccias, dips in some coarse, clast-supported block-and-boulder sediments at Fossil Rock, and some gently sloping, ridge-capping lava flows that suggest they may be remnants of shield-volcano flanks in and south of the map area. Clusters of measured orientations document different trends in different parts of the map, and Schasse (1987) reported measurements that imply additional differences. Joints—which we mapped anywhere we saw orderly sets—are likewise varied, and joints near the southwestern map corner differ from nearby joints west of the map. The differences suggest some structural complexity, and absent other data, we used them to help inform cross-section A–A', but we feel the existing data are insufficient for specific structural inferences. A possible exception may be localized variations about 600 m southwest of the northwest-striking, queried fault between Green Hill and Bald Hill (discussed below).

Unit RMc

A westward apparent dip of 1–4 degrees, intermittently exposed in broad cliffs along 3 km of Nisqually River valley west of geochemistry site GD6, is mostly post-depositional because it tilts peats and lacustrine beds. But the dip need not be tectonic—compaction of Tacoma Basin fill may explain it.

FAULTS

Olympia fault

Northwest-striking strands of the Olympia fault ('OF' in Fig. M1A) follow gravity and magnetic gradients that enter the Bald Hill quadrangle from the west (Polenz and others, 2022) but then widen into a patchwork of weak curvilinear gradients ('CLG' in Fig. M1A) that range in orientation from west to north and northeast. We interpret the transition to these weak gradients as the likely termination of the Olympia fault ('T' on Fig. M1A). Gravity contours east of the Olympia fault define a gradual or stepped slope into the Tacoma basin, and weak max-spot clusters ('NF' in Fig. M1A) may mark smaller normal faults (Fig. M1B). The northwest-striking fault between Bald and Green hills

(discussed below) is the only feature with notable corroborating geologic evidence.

Fault east of Green Hill

Three northeast-striking fault strands in one outcrop east of Green Hill together have ~7 m southeast-down offset (Fig. 7). A gently plunging slickenline combined with the observed offset implies left-lateral slip, possibly with a southeast-down normal component.

Fault between Bald Hill and Green Hill

We suggest a northwest-striking fault across the center of the map because several individually unremarkable features align along a roughly 9 km-long, straight, northwesterly trend, including: straight valley reaches along the Deschutes River and on both sides of a ridge northwest thereof; a saddle on that ridge; three mid-slope closed depressions (that could be glacially influenced) along the valley northwest of the saddle; and a line of aeromagnetic max-spots from there northwest across Elbow Lake (SML in Fig. M1A). A similar line of aeromagnetic max-spots along the Deschutes River valley segment of the postulated fault may be caused by topography cutting layers of magnetic volcanics at the surface.

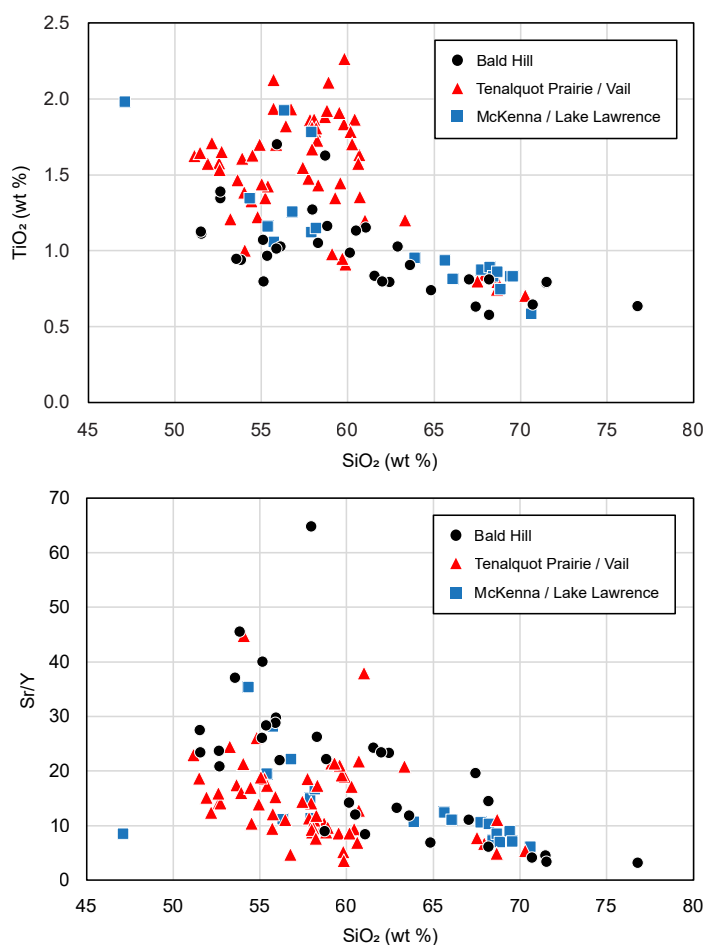


Figure 6. Harker variation diagrams illustrating chemical contrasts among Northcraft Formation samples from this study (Bald Hill) versus samples from the Tenalquot Prairie and Vail quadrangles (Polenz and others, 2021) and the McKenna and Lake Lawrence quadrangles (Polenz and others, 2022).



Figure 7. View to the south showing a fault east of Green Hill along Weyerhaeuser ‘bypass’ road cut. Note the sharp contact (at level of geologist Frank Hladky’s hands) between the pinkish paleosol and the overlying gray andesite flow, and the southeast-down offset in left center of image.

Nearly all bedding orientations within 1 km southwest of the postulated fault strike roughly fault-parallel and dip gently southwest, whereas those northeast of it are more varied. Structures on both sides of the postulated fault share its northwesterly orientation, suggesting a potentially wider zone with multiple strands. These include a small fault surface striking 312 degrees and dipping 84 degrees northeast approximately 110 m northeast of the postulated fault (near geochemistry site G18) and localized bedding dip changes observed at two sites 600 m west of the postulated fault—at the top of Green Hill and 2.2 km farther northwest (just east of geochemistry site G14). If the postulated fault exists, a lack of deflection across the ridge northeast of the Deschutes River valley segment suggests a near-vertical fault plane. Although the postulated fault parallels the Olympia fault, it is mid-basin and oriented perpendicular to gravity contours and therefore must not have much basement offset.

We suspect that the postulated fault has not been post-glacially active: the closed depressions on the north-facing slope northwest of Green Hill may be glacially influenced, and we observed no candidate fault scarps in the Vashon Drift farther northwest.

GEOPHYSICAL MODELING

Tacoma Basin edge

Our two-dimensional forward modeling of aeromagnetic and gravity data along line X–X’ (Fig. M1A) is collocated with Cross Section A–A’ in the map area and indicates multi-kilometer-scale north-down displacement of mafic igneous basement (Crescent Formation in Figs. M1B, C) at the southern margin of the Tacoma basin east of the Olympia fault. Based on physical property analyses (see *Methods*, Appendix C) and prior modeling nearby (Polenz and others, 2021, 2022), we estimate a ρ of 2,295–2,380 kg/m³ for interbedded volcanoclastic rocks, andesite, and sedimentary rocks (together approximated by unit Evc_N in Cross Section A–A’) and 2,880 kg/m³ for Crescent Formation. In our models, this density contrast reproduces most of the observed gravity gradient (Figs. M1B, C).

We present two geophysical models with differing solutions that fit our observed data equally well: a fault-bounded margin (Fig. M1B) and a fold-bounded margin (Fig. M1C). While geophysical modeling does not require faulting to match observed fields, it does require a north-down basin edge. We prefer the faulted solution for the following reasons. A faulted basin edge is consistent with previous geophysical model solutions of Polenz and others (2021, 2022). Faulting would have provided weak points in the crust that preferentially allow magma to intrude, explaining our observations of intrusives at the surface (Eid_N in M1B). The normal faults we modeled (‘NF’ in Fig M1A) may be splay faults related to the possible termination of the Olympia Fault (‘T’ in Fig M1A), as suggested by the gravity max spots. Similar Eocene-aged basins are fault bounded farther south in the Washington forearc (Van Wagoner and others, 2002). We note that all field-observed dikes trend east–west and appear to be Northcraft Formation, consistent with Eocene north–south extension and the normal faults in model M1B.

Tacoma Basin fill

We model Tacoma basin fill as sedimentary and volcanic rocks thickening into the basin northeast of the Olympia fault. We interpret all basin fill below ~180 m (600 ft) underground as Northcraft Formation-age or older (units Evc_N, Eva_N, and Ens, Figs. M1B, C) because at the southern end of the basin, mapped and dated Northcraft Formation overlies these deeper deposits. Shallow, magnetic volcanic rocks (which we interpret as Northcraft andesite flows) could be interlayered with volcanoclastic rocks at depth, and thus extend deeper into the subsurface. The magnetic volcanic rocks shown in the shallow subsurface must exist in order to fit the magnetic data and maintain a geologically reasonable geometry for the deposits. We infer syn-depositional basin formation (see also Polenz and others, 2021, 2022).

Above ~180 m (600 ft) underground, the Willhoite well (located 6.6 km north of the map area; Fig. M1A) and our modeling support sediment with lower density and magnetic susceptibility (Fig. M1B, C; units ØEn and RMc in Cross Section A–A’). The thicknesses of units RMc and ØEn are poorly constrained by the gravity and magnetics, therefore their combined thickness in Cross Section A–A’ is mostly based on the observed section in the Willhoite well.

Tacoma Basin volcanism and intrusions

High-amplitude long-wavelength aeromagnetic anomalies support widespread, strongly magnetic deep-subsurface rocks (‘TBV’ in Figs. M1B, C; Polenz and others, 2021, 2022; Contreras and others, 2023) beneath Quaternary sediment and geological map unit Ens between the mountains and the Nisqually River. Shorter-wavelength aeromagnetic highs at Bald and Green Hills and the southeastern map corner (MV in Fig. M1A) suggest shallow intrusions (units Eii_N and Eid_N in Figs. M1B, C; unit Eii_N in Cross Section A–A’). The gravity and magnetic data did not require intrusion CI (Fig. M1) to extend deeper into the basin, therefore we suggest the source for these rocks is northeast of the cross section. These intrusions add support to our field-based interpretation and prior inferences (Snively and others, 1958; Polenz and others, 2021, 2022) that the Northcraft Formation includes multiple volcanic centers in and near the map area.

SUGGESTIONS FOR FURTHER STUDY

- Firmly link specific geologic unit(s) to aquifer(s) with elevated arsenic content by: checking wells in Thurston County for elevated arsenic content; studying in detail driller's logs from wells that produce water with elevated arsenic content; identifying geologic units of cuttings during construction of new wells; and assessing potentially related observations (such as Walters and Kimmel's (1968) note on geographic distribution of wells with elevated bicarbonate content), geochemical conditions, and processes in affected wells.
- Study in detail features along the questionably inferred fault between Bald Hill and Green Hill to test its existence and shed light on its character.
- Collect and analyze additional gravity data south of the map area to test if the Olympia fault really terminates in the map area.
- Identify near surface structures proximal to zones of elevated arsenic.
- Assess unit RMc leaf fossil content at age site GD16, compare to Mashel Formation, and acquire chronometric age control from the Mashel Formation type section to test correlation of these similar deposits.
- Collect, assemble, and compare additional geological, geochemical, paleontological, and radiometric data from the early Cascade arc and related units to better understand the arc's evolution and improve correlations between geologic units in or related to the arc.

ACKNOWLEDGMENTS

We thank: Pat Pringle and Tim Walsh (both WGS retired) and Jim Vallance (USGS) for insights related to Quaternary lahar deposits; Jim Vallance and Madelyn Cook (USGS) for analysis of pumice from one lahar deposit; Christopher Schiller (Burke Museum) for analysis of fossil pollen; Paul Kester (Burke Museum) for processing of plant fossils; Ruth Martin (Burke Museum) for analysis of foraminifera; Michael Nesbitt for assistance with fossil sampling; Megan Anderson (WGS) for guidance on geophysical data collection, modeling, and interpretation; Trevor Contreras, Rebecca Goughnour, and Alex Steely (WGS) for assistance with some field work; all WGS staff who provided suggestions, edits, and guidance; Weyerhaeuser Company, Manke Lumber Company, the Pack Forest, the cities of Centralia and Tacoma, the Nisqually Land Trust, Wilcox Family Farms, and countless other landowners for access, local knowledge, historical context, well records, and other information.

WORKER CONTRIBUTIONS

A. Bauer performed and T. Lau directed geophysical modeling. A. Bauer and T. Lau performed geophysical data collection. F. Hladky carried out most bedrock geologic fieldwork and all petrography and clast counts, and he drafted some pamphlet text and greatly contributed edits and reviews for its entirety. G. Legorreta Paulín provided Landsat data analysis. E. Nesbitt

conducted and delegated fossil identifications, related paleoenvironmental interpretations, and biostratigraphic assessments. M. Polenz functioned as project lead, drafted GIS features and the overall report, and led Quaternary geologic fieldwork. J. Tepper analyzed geochemistry, prepared the geochemical data supplement, and drafted the geochemical discussion.

REFERENCES

- Ali, A. E.; El Khidir, S. O.; Babikir, I. A. A.; Abdelrahman, E. M., 2012, Landsat ETM+ 7 digital image processing techniques for lithological and structural lineament enhancement: Case study around Abidiya Area, Sudan: *The Open Remote Sensing Journal*, v. 5, p. 83–89. [<https://doi.org/10.2174/1875413901205010083>]
- Barnes, D. F.; Oliver, H. W.; Robbins, S. L., 1969, Standardization of gravimeter calibrations in the Geological Survey: *Eos Transactions*, v. 50, no. 10, p. 626–627. [<https://doi.org/10.1029/EO050i010p00526>]
- Black, L. P.; Kamo, S. L.; Allen, C. M.; Davis, D. W.; Aleinikoff, J. N.; Valley, J. W.; Mundil, Roland; Campbell, I. H.; Korsch, R. J.; Williams, I. S.; Foudoulis, Chris, 2004, Improved $^{206}\text{Pb}/^{238}\text{U}$ microprobe geochronology by the monitoring of a trace-element-related matrix effect; SHRIMP, ID-TIMS, ELA-ICP-MS and oxygen isotope documentation for a series of zircon standards: *Chemical Geology*, v. 205, p. 115–140. [<https://doi.org/10.1016/j.chemgeo.2004.01.003>]
- Blakely, R. J.; Jachens, R. C., 1990, Volcanism, isostatic residual gravity, and regional tectonic setting of the Cascade volcanic province: *Journal of Geophysical Research Solid Earth*, vol. 95, no. B12, p. 19,439–19,451. [<https://doi.org/10.1029/JB095iB12p19439>]
- Blakely, R. J.; Wells, R. E.; Weaver, C. S., 1999, Puget Sound aeromagnetic maps and data: U.S. Geological Survey Open-File Report 99-514, version 1.0. [<http://geopubs.wr.usgs.gov/open-file/of99-514/>]
- Blakely, R. J.; Sherrod, B. L.; Weaver, C. S., 2020, High-resolution aeromagnetic survey of the Centralia area, southwest Washington: U.S. Geological Survey data release. [<https://doi.org/10.5066/P9T4UC6W>]
- Booth, D. B.; Troost, K. G.; Clague, J. J.; Waitt, R. B., 2004, The Cordilleran ice sheet. In Gillespie, A. R.; Porter, S. C.; Atwater, B. F., editors, *The Quaternary period in the United States*: Elsevier, p. 17–43.
- Bretz, J. H., 1911, The terminal moraine of the Puget Sound glacier: *Journal of Geology*, v. 19, no. 2, p. 161–174. [<https://doi.org/10.1086/621826>]
- Bretz, J. H., 1913, Glaciation of the Puget Sound region: Washington Geological Survey Bulletin 8, 244 p., 3 plates. [http://www.dnr.wa.gov/publications/ger_b8_glaciation_pugetsound.pdf]
- Brocher, T. M.; Parsons, T. E.; Blakely, R. J.; Christensen, N. I.; Fisher, M. A.; Wells, R. E.; SHIPS Working Group, 2001, Upper crustal structure in Puget Lowland, Washington: Results from the 1998 Seismic Hazards Investigations in Puget Sound: *Journal of Geophysical Research Solid Earth*, v. 106, no. B7, p. 13,541–13,564. [<https://doi.org/10.1029/2001JB000154>]
- Brown, N. E.; Hallet, Bernard; Booth, D. B., 1987, Rapid soft bed sliding of the Puget glacial lobe: *Journal of Geophysical Research Solid Earth*, v. 92, no. B9, p. 8985–8997. [<https://doi.org/10.1029/JB092iB09p08985>]
- Brown, Olivia; Harris, J. R.; Utting, Daniel; Little, E. C., 2007, Remote predictive mapping of surficial materials on northern Baffin Island: developing and testing techniques using Landsat TM and digital elevation data: *Geological Survey of Canada Current Research 2007-B1*, 12 p.

- Buckovic, W. A., 1979, The Eocene deltaic system of west-central Washington. *In* Armentrout, J. M.; Cole, M. R.; Ter Best, Harry, Jr., editors, Cenozoic paleogeography of the western United States: Society of Economic Paleontologists and Mineralogists Pacific Section, Pacific Coast Paleogeography Symposium 3, p. 147–163.
- Chang, Zhaoshan; Vervoort, J. D.; McClelland, W. C.; Knaack, Charles, 2006, U-Pb dating of zircon by LA-ICP-MS: Geochemistry, Geophysics, Geosystems, v. 7, p. Q05009. [https://doi.org/10.1029/2005GC001100]
- Christiansen, R. L.; Calvert, A. T.; Grove T. L., 2017, Geologic field-trip guide to Mount Shasta volcano, northern California: U.S. Geological Survey Scientific Investigations Report 2017-5022-K3, 33 p. [https://doi.org/10.3133/sir20175022K3]
- Clement, C. R.; Pratt, T. L.; Holmes, M. L.; Sherrod, B. L., 2010, High-resolution seismic reflection imaging of growth folding and shallow faults beneath the southern Puget Lowland, Washington State: Bulletin of the Seismological Society of America, v. 100, no. 4, p. 1710–1723. [https://doi.org/10.1785/0120080306]
- Contreras, T. A.; Goughnour, R. L.; Lau, T. R., 2023, Geologic map of the Harts Lake 7.5-minute quadrangle, Pierce and Thurston Counties, Washington: Washington Geological Survey Map Series 2023-04, 1 sheet, scale 1:24,000, with 16 p. text. [https://www.dnr.wa.gov/publications/ger_ms2023-04_geol_map_harts_lake_24k.zip]
- Crandell, D. R.; Miller, R. D., 1974, Quaternary stratigraphy and extent of glaciation in the Mount Rainier region, Washington: U.S. Geological Survey Professional Paper 847, 59 p., 2 plates. [https://doi.org/10.3133/pp847]
- Czajkowski, J. L., 2016, Washington State geochronology database—GIS data: Washington Division of Geology and Earth Resources Digital Data Series 6, version 1.1, originally released November, 2014.
- Daneš, Z. F.; Bonno, M. M.; Brau, E.; Gilham, W. D.; Hoffman, T. F.; Johansen, D.; Jones, M. H.; Malfait, B.; Masten, J.; Teague, G. O., 1965, Geophysical investigation of the southern Puget Sound area, Washington: Journal of Geophysical Research Solid Earth, v. 70, no. 22, p. 5573–5580. [https://doi.org/10.1029/JZ070i022p05573]
- Daneš, Z. F., 1985, Sedimentary thickness in the Puget Sound area, Washington, derived from aeromagnetic data: Washington Division of Geology and Earth Resources Open File Report 85-5, 14 p. [http://www.dnr.wa.gov/publications/ger_ofr85-5_puget_sound_sediment_thickness.pdf]
- Drost, B. W.; Ely, D. M.; Lum, W. E., II, 1999, Conceptual model and numerical simulation of the ground-water-flow system in the unconsolidated sediments of Thurston County, Washington: U.S. Geological Survey Water-Resources Investigations Report 99-4165, 254 p. [http://pubs.er.usgs.gov/publication/wri994165]
- Eddy, M. P.; Bowring, S. A.; Umhoefer, P. J.; Miller, R. B.; McLean, N. M.; Donaghy, E. E., 2016, High-resolution temporal and stratigraphic record of Siletzia's accretion and triple junction migration from nonmarine sedimentary basins in central and western Washington: Geological Society of America Bulletin, v. 128, no. 3/4, p. 425–441. [https://doi.org/10.1130/B31335.1]
- Eddy, M. P.; Clark, K. P.; Polenz, Michael, 2017, Age and volcanic stratigraphy of the Eocene Siletzia oceanic plateau in Washington and on Vancouver Island: Lithosphere, v. 9, no. 4, p. 652–664. [https://doi.org/10.1130/L650.1]
- Finn, C. A., 1990, Geophysical constraints on Washington convergent margin structure: Journal of Geophysical Research, v. 95, no. B12, p. 19,533–19,546. [https://doi.org/10.1029/JB095iB12p19533]
- Finn, C. A.; Phillips, W. M.; Williams, D. L., 1991, Gravity anomaly and terrain maps of Washington: U.S. Geological Survey Geophysical Investigations Map GP-988, 5 sheets, scale 1:500,000. [https://doi.org/10.3133/gp988]
- Flores, R. M.; Johnson, S. Y., 1995, Sedimentology and lithofacies of the Eocene Skookumchuck Formation in the Centralia coal mine, southwest Washington. *In* Fritsche, A. E., editor, Cenozoic paleogeography of the western United States—II: Society for Sedimentary Geology (SEPM) Pacific Section Book 75, p. 274–290.
- Folk, R. L., 1980, Petrology of sedimentary rocks: Hemphill Publishing Company, 182 p.
- Gard, L. M., Jr., 1968, Bedrock geology of the Lake Tapps quadrangle, Pierce County, Washington: U.S. Geological Survey Professional Paper 388-B, 33 p., 2 plates. [http://pubs.er.usgs.gov/usgspubs/pp/pp388B]
- Gaschnig, R. M.; Vervoort, J. D.; Lewis, R. S.; McClelland, W. C., 2010, Migrating magmatism in the northern US Cordillera: in situ U–Pb geochronology of the Idaho batholith: Contributions to Mineralogy and Petrology, v. 159, p. 863–883. [https://doi.org/10.1007/s00410-009-0459-5]
- Gower, H. D.; Yount, J. C.; Crosson, R. S., 1985, Seismotectonic map of the Puget Sound region, Washington: U.S. Geological Survey Miscellaneous Investigations Series Map I-1613, 1 sheet, scale 1:250,000, with 15 p. text. [https://doi.org/10.3133/i1613]
- Hagen, R. A., 1987, The geology and petrology of the Northcraft Formation, Lewis County, Washington: University of Oregon Master of Science thesis, 252 p., 1 plate.
- Haugerud, R. A., 2009, Preliminary geomorphic map of the Kitsap Peninsula, Washington; version 1.0: U.S. Geological Survey Open-File Report 2009-1033, 2 sheets, scale 1:36,000. [https://pubs.usgs.gov/of/2009/1033/]
- Haugerud, R. A., 2021, Deglaciation of the Puget Lowland, Washington. *In* Waitt, R. B.; Thackray, G. D.; Gillespie, A. R., editors, Untangling the Quaternary period—a legacy of Stephen C. Porter: Geological Society of America Special Paper 548, p. 279–298. [https://doi.org/10.1130/2020.2548(14)]
- Heiskanen, W. A.; Vening-Meinesz, F. A., 1958, The Earth and its gravity field: McGraw-Hill Book Company, Inc., 470 p.
- Hladky, F. R., 1998, Age, chemistry, and origin of capping lava at Upper Table Rock and Lower Table Rock, Jackson County, Oregon: Oregon Geology, v. 60, no. 4, p. 81–91.
- International Union of Geodesy and Geophysics, 1971, Geodetic Reference System 1967: International Association of Geodesy Special Publication no. 3, 116 p.
- Irvine, T. N.; Baragar, W. R. A., 1971, A guide to the chemical classification of the common volcanic rocks: Canadian Journal of Earth Sciences, v. 8, no. 5, p. 523–548. [https://doi.org/10.1139/e71-055]
- Irving, A. J.; Nesbitt, E. A.; Renne, P. R., 1996, Age constraints on earliest Cascade arc volcanism and Eocene marine biozones from a feldspar-rich tuff in the Cowlitz Formation, southwestern Washington [abstract]: Eos, Transactions of the American Geophysical Union, v. 77, no. 46, Supplement, p. F814.
- Koppers, A. A. P.; Staudigel, Hubert; Wijbrans, J. R., 2000, Dating crystalline groundmass separates of altered Cretaceous seamount basalts by the $^{40}\text{Ar}/^{39}\text{Ar}$ incremental heating technique, Chemical Geology, vol. 166, p. 139–158. [https://doi.org/10.1016/S0009-2541(99)00188-6]
- Koppers, A. A. P., 2002, ArArCALC—Software for $^{40}\text{Ar}/^{39}\text{Ar}$ age calculations: Computers and Geosciences, vol. 28, p. 605–619. [https://doi.org/10.1016/S0098-3004(01)00095-4]
- Koppers, A. A. P.; Staudigel, Hubert; Malcolm, S. P.; Wijbrans, J. R., 2003, Short-lived and discontinuous intraplate volcanism in the South Pacific: Hot spots or extensional volcanism?: Geochemistry, Geophysics, Geosystems, v. 4, no. 10. [https://doi.org/10.1029/2003GC000533]
- Kuiper, K. F.; Deino, Alan; Hilgen, F. J.; Krijgsman, Wout; Renne, P. R.; Wijbrans, J. R., 2008, Synchronizing rock clocks of earth history: Science, v. 320, no. 5875, p. 500–504. [https://doi.org/10.1126/science.1154339]

- Kettles, I. M.; Rencz, A. N.; Bauke, S. D., 2000, Integrating Landsat, geologic, and airborne gamma ray data as an aid to surficial geology mapping and mineral exploration in the Manitouwadge area, Ontario: Photogrammetric Engineering & Remote Sensing, v. 66, no. 4, p. 437–445.
- Lanphere, M. A.; Baadsgaard, Halfdan, 2001, Precise K–Ar, $^{40}\text{Ar}/^{39}\text{Ar}$, Rb–Sr and U/Pb mineral ages from the 27.5 Ma Fish Canyon Tuff reference standard: Chemical Geology, vol. 175, issues 3–4. [https://doi.org/10.1016/S0009-2541(00)00291-6]
- Le Bas, M. J.; Le Maitre, R. W.; Streckeis, A. L.; Zanettin, Bruno, 1986, A chemical classification of volcanic rocks based on the total alkali-silica diagram: Journal of Petrology, v. 27, no. 3, p. 745–750. [https://doi.org/10.1093/petrology/27.3.745]
- Lee, J. Y.; Marti, Kurt; Severinghaus, J. P.; Kawamura, Kenji; Yoo, Hee-Soo; Lee, J. B.; Kim, J. S., 2006, A redetermination of the isotopic abundances of atmospheric Ar: Geochimica et Cosmochimica Acta, v. 70, no. 17, p. 4507–4512. [https://doi.org/10.1016/j.gca.2006.06.1563]
- Lisiecki, L. E.; Raymo, M. E., 2005, A Pliocene-Pleistocene stack of 57 globally distributed benthic $\delta^{18}\text{O}$ records: Paleoclimatology, v. 20, no. 1, 17 p. [https://doi.org/10.1029/2004PA001071]
- Logan, R. L.; Walsh, T. J.; Stanton, B. W.; Sarikhan, I. Y., 2009, Geologic map of the Maytown 7.5-minute quadrangle, Thurston County, Washington: Washington Division of Geology and Earth Resources Geologic Map GM-72, 1 sheet, scale 1:24,000. [http://www.dnr.wa.gov/Publications/ger_gm72_geol_map_maytown_24k.pdf]
- Ludwig, K. R., 2003, Isoplot 3.00: A geochronological toolkit for Microsoft Excel: Berkeley Geochronology Center, Berkeley, 70 p.
- Madin, I. P.; Murray, R. B.; Hladky, F. R., 2006, Preliminary geologic map of the Coburg 7.5' quadrangle, Lane and Linn Counties, Oregon: Oregon Department of Geology and Mineral Industries Open File Report O-06-06, 2 sheets, scale 1:25,000, with 24 p. text. [https://www.oregongeology.org/pubs/ofr/O-06-06.zip]
- Magsino, Sammantha; Sanger, Elizabeth; Walsh, T. J.; Palmer, S. P.; Blakely, R. J., 2003, The Olympia structure: Ramp or discontinuity? New gravity data provide more information [abstract]: Geological Society of America Abstracts with Programs, v. 35, no. 6, p. 479. [https://gsa.confex.com/gsa/2003AM/webprogram/Paper67057.html]
- McBirney, A. R., 1978, Volcanic evolution of the Cascade Range: Annual Reviews of Earth and Planetary Sciences, v. 6, p. 437–456. [https://doi.org/10.1146/annurev.ea.06.050178.002253]
- McCaffrey, Robert; King, R. W.; Payne, S. J.; Lancaster, Matthew, 2013, Active tectonics of northwestern U.S. inferred from GPS-derived surface velocities: Journal of Geophysical Research Solid Earth, v. 118, no. 2, p. 709–723. [https://doi.org/10.1029/2012JB009473]
- Min, Kyoungwon; Mundil, Roland; Renne, P. R.; Ludwig, K. R., 2000, A test for systematic errors in $^{40}\text{Ar}/^{39}\text{Ar}$ geochronology through comparison with U–Pb analysis of a 1.1-Ga rhyolite: Geochimica et Cosmochimica Acta, v. 64, p. 73–98. [https://doi.org/10.1016/S0016-7037(99)00204-5]
- Morelli, Carlo, editor, 1974, The International Gravity Standardization Net, 1971: International Association of Geodesy Special Publication no. 4, 194 p.
- Morrison, R. B., 1991, Introduction. In Morrison, R. B., editor, Quaternary nonglacial geology—Conterminous U.S.: Geological Society of America, Decade of North American Geology, The Geology of North America, v. K-2, p. 1–12.
- Mundorff, M. J.; Weigle, J. M.; Holmberg, G. D., 1955, Ground water in the Yelm area, Thurston and Pierce Counties, Washington: U.S. Geological Survey Circular 356, 58 p., 2 plates. [http://pubs.er.usgs.gov/publication/cir356]
- Nelson, A. R.; Personius, S. F.; Sherrod, B. L.; Buck, Jason; Bradley, Lee-Ann; Henley, Gary, II; Liberty, L. M.; Kelsey, H. M.; Witter, R. C.; Koehler, R. D.; Schermer, E. R.; Nemser, E. S.; Cladouhos, T. T., 2008, Field and laboratory data from an earthquake history study of scarps in the hanging wall of the Tacoma fault, Mason and Pierce Counties, Washington: U.S. Geological Survey Scientific Investigations Map 3060, 3 sheets, scale 1:30,000. [http://pubs.usgs.gov/sim/3060/]
- Nilsen, T. H., 1976, Washington gravity base station network: Washington Division of Geology and Earth Resources Information Circular 59, 83 p. [http://www.dnr.wa.gov/Publications/ger_ic59_wa_gravity_base_network.pdf]
- Noble, J. B.; Wallace, E. F., 1966, Geology and ground-water resources of Thurston County, Washington; Volume 2: Washington Division of Water Resources Water Supply Bulletin 10, v. 2, 141 p., 5 plates. [https://apps.ecology.wa.gov/publications/SummaryPages/WSB10b.html]
- Odum, J. K.; Stephenson, W. J.; Pratt, T. L.; Blakely, R. J., 2016, Shallow geophysical imaging of the Olympia anomaly: An enigmatic structure in the southern Puget Lowland, Washington State: Geosphere, v. 12, no. 5, p. 1617–1632. [https://doi.org/10.1130/GES01248.1]
- Paces, J. B.; Miller, J. D., Jr., 1993, Precise U–Pb ages of Duluth Complex and related mafic intrusions, northeastern Minnesota: Geochronological insights to physical, petrogenetic, paleomagnetic, and tectonomagmatic processes associated with the 1.1 Ga Midcontinent Rift System: Journal of Geophysical Research Solid Earth, v. 98, p. 13,997–14,013. [https://doi.org/10.1029/93JB01159]
- Parker, B. L.; Goldstein, B. S.; Futornick, Z. O.; Pringle, P. T., 2008, Sedimentological evidence for an enriched glacial outburst flood in Thurston County, Washington [abstract]: Geological Society of America Abstracts with Programs, v. 40, no. 1, p. 70.
- Paton, Chad; Hellstrom, John; Paul, Bence; Woodhead, Jon; Hergt, Janet, 2011, Iolite: Freeware for the visualisation and processing of mass spectrometric data: Journal of Analytical Atomic Spectrometry, v. 26, p. 2508–2518. [https://doi.org/10.1039/C1JA10172B]
- Pease, M. H., Jr.; Hoover, Linn, Jr., 1957, Geology of the Doty-Minot Peak area, Washington: U.S. Geological Survey Oil and Gas Investigations Map 188, 1 sheet, scale 1:62,500. [https://ngmdb.usgs.gov/Prodesc/proddesc_5340.htm]
- Peck, D. L.; Griggs, A. B.; Schlicker, H. G.; Well, F. G.; Dole, H. M., 1964, Geology of the central and northern parts of the Western Cascade Range in Oregon: U.S. Geological Survey Professional Paper 449, 56 p., 1 plate. [https://pubs.er.usgs.gov/publication/pp449]
- Phillips, W. M.; Korosec, M. A.; Schasse, H. W.; Anderson, J. L.; Hagen, R. A., 1986, K–Ar ages of volcanic rocks in southwest Washington: Isochron/West, Bulletin of Isotopic Geochronology, v. 47, p. 18–24.
- Phillips, W. M.; Walsh, T. J.; Hagen, R. A., 1989, Eocene transition from oceanic to arc volcanism, southwest Washington. In Muffler, L. J. P.; Weaver, C. S.; Blackwell, D. D., editors, Proceedings of workshop XLIV: Geological, geophysical, and tectonic setting of the Cascade Range: U.S. Geological Survey Open-File Report 89-178, p. 199–256. [https://doi.org/10.3133/ofr89178]
- Phillips, J. D.; Hansen, R. O.; Blakely, R. J., 2007, The use of curvature in potential-field interpretation: Exploration Geophysics, v. 38, p. 111–119. [https://doi.org/10.1071/EG07014]
- Pierce County, WA, 2020, Pierce 2020 project, Pierce County, WA Lidar 2020, collected between April 10 and June 3, 2020 by Sanborn Map Company, Inc., 3-ft resolution, accessed April 16, 2023 [http://lidarportal.dnr.wa.gov/], metadata available on portal [https://lidarportal.dnr.wa.gov/download?ids=1487].
- Plouff, Donald, 2000, Field estimates of gravity terrain corrections and Y2K-compatible method to convert from gravity readings with multiple base stations to tide- and long-term drift-corrected observations: U.S. Geological Survey Open-File Report 2000-140, 35 p. [https://doi.org/10.3133/ofr00140]

- Polenz, Michael; Alldritt, Katelin; Hehemann, N. J.; Sarikhan, I. Y.; Logan, R. L., 2009, Geologic map of the Belfair 7.5-minute quadrangle, Mason, Kitsap, and Pierce Counties, Washington: Washington Division of Geology and Earth Resources Open File Report 2009-7, 1 sheet, scale 1:24,000. [http://www.dnr.wa.gov/Publications/ger_ofr2009-7_geol_map_belfair_24k.pdf]
- Polenz, Michael; Petro, G. T.; Contreras, T. A.; Stone, K. A.; Legorreta Paulín, Gabriel; Cakir, Recep, 2013, Geologic map of the Seabeck and Poulsbo 7.5-minute quadrangles, Kitsap and Jefferson Counties, Washington: Washington Division of Geology and Earth Resources Map Series 2013-02, 1 sheet, scale 1:24,000, 39 p. text. [https://www.dnr.wa.gov/Publications/ger_ms2013-02_geol_map_seabeck-poulsbo_24k.zip]
- Polenz, Michael; Favia, J. G.; Hubert, I. J.; Legorreta Paulín, Gabriel; Cakir, Recep, 2015, Geologic map of the Port Ludlow and southern half of the Hansville 7.5-minute quadrangles, Kitsap and Jefferson Counties, Washington: Washington Division of Geology and Earth Resources Map Series 2015-02, 1 sheet, scale 1:24,000, 40 p. text. [http://www.dnr.wa.gov/publications/ger_ms2015-02_geol_map_port_ludlow_hansville_24k.zip]
- Polenz, Michael; Allen, M. D.; Legorreta Paulín, Gabriel; Eungard, D. W.; Cakir, Recep; Scott, S. P.; Mahan, S. A., 2016, Geologic map of the Shelton Valley 7.5-minute quadrangle, Mason County, Washington: Washington Division of Geology and Earth Resources Map Series 2016-02, 1 sheet, scale 1:24,000, 45 p. text. [http://www.dnr.wa.gov/publications/ger_ms2016-02_geol_map_shelton_valley_24k.zip]
- Polenz, Michael; Vermeer, J. L.; Legorreta Paulín, Gabriel; Tepper, J. H.; Mahan, S. A.; Cakir, Recep, 2017, Geologic map of the Littlerock 7.5-minute quadrangle, Thurston County, Washington: Washington Geological Survey Map Series 2017-01, 1 sheet, scale 1:24,000, 36 p. text. [https://www.dnr.wa.gov/publications/ger_ms2017-01_geol_map_littlerock_24k.zip]
- Polenz, Michael; Ostrom, B. A.; Lau, T. R.; Sadowski, A. J.; Blanks-Bennett, A. L.; Cakir, Recep; Tepper, J. H.; Legoretta Paulín, Gabriel; Nesbitt, Elizabeth; DuFrane, S. A., 2018, Geologic map of the Violet Prairie 7.5-minute quadrangle, Thurston and Lewis Counties, Washington: Washington Geological Survey Map Series 2018-04, 1 sheet, scale 1:24,000, 41 p. text. [https://www.dnr.wa.gov/publications/ger_ms2018-04_geol_map_violet_prairie_24k.zip]
- Polenz, Michael; Samson, Catherine; Reedy, Tabor; von Dassow, Wesley; Duckworth, C. W.; Lau, T. R.; Anderson, M. L.; Nesbitt, E. A.; Tepper, J. H.; DuFrane, S. A.; Legorreta Paulín, Gabriel, 2020, Geologic map of the Oakville and Rainbow Falls 7.5-minute quadrangles, Lewis, Thurston, and Grays Harbor Counties, Washington: Washington Geological Survey Map Series 2020-02, 1 sheet, scale 1:24,000, 19 p. text. [https://www.dnr.wa.gov/publications/ger_ms2020-02_geol_map_oakville_rainbow_falls_24k.zip]
- Polenz, Michael; Hladky, F. R.; Anderson, M. L.; Tepper, J. H.; Horst, A. E.; Miggins, D. P.; Legoretta Paulín, Gabriel, 2021, Geologic map of the Tenalquot Prairie and northern two-thirds of the Vail 7.5-minute quadrangles, Thurston and Pierce Counties, Washington: Washington Geological Survey Map Series 2021-02, 1 sheet, scale 1:24,000, 47 p. text. [https://www.dnr.wa.gov/publications/ger_ms2021-02_geol_map_tenalquot_prairie_northern_vail_24k.zip]
- Polenz, Michael; Hladky, F. R.; Anderson, M. L.; Alexander, K. A.; Tepper, J. H.; Miggins, D. P.; Legoretta Paulín, Gabriel, 2022, Geologic map of the McKenna and northern half of the Lake Lawrence 7.5-minute quadrangles, Thurston and Pierce Counties, Washington: Washington Geological Survey Map Series 2022-06, 1 sheet, scale 1:24,000, 35 p. text. [https://www.dnr.wa.gov/publications/ger_ms2022-06_geol_map_mckenna_northern_lake_lawrence_24k.zip]
- Pratt, T. L.; Johnson, S. Y.; Potter, C. J.; Stephenson, W. J.; Finn, C. A., 1997, Seismic reflection images beneath Puget Sound, western Washington State: The Puget Lowland thrust sheet hypothesis: *Journal of Geophysical Research Solid Earth*, v. 102, no. B12, p. 27,469–27,489. [<https://doi.org/10.1029/97JB01830>]
- Pringle, P. T., 1990, The Nisqually landslide of September 1990: *Washington Geologic Newsletter*, v. 18, no. 4, p. 28–31. [https://www.dnr.wa.gov/Publications/ger_washington_geology_1990_v18_no4.pdf]
- Pringle, P. T.; Goldstein, B. S., 2002, Deposits, erosional features, and flow characteristics of the late-glacial Tanwax Creek–Ohop Creek Valley flood—A likely source for sediments composing the Mima Mounds, Puget Lowland, Washington [abstract]: *Geological Society of America Abstracts with Programs*, v. 34, no. 5, p. A-89.
- Puget Sound Regional Council, 2005, Puget Lowlands 2005 project, collected in 2005 by Terrapoint, 3-ft resolution, accessed April 16, 2023 [<http://lidarportal.dnr.wa.gov/>], metadata available on portal [<https://lidarportal.dnr.wa.gov/download?ids=864>].
- Sadowski, A. J.; Keller, W. E.; Polenz, Michael; Lau, T. R.; Cakir, Recep; Nesbitt, Elizabeth; Tepper, J. H.; DuFrane, S. A.; Legoretta Paulín, Gabriel, 2018, Geologic map of the Centralia 7.5-minute quadrangle, Lewis County, Washington: Washington Geological Survey Map Series 2018-05, 1 sheet, scale 1:24,000, 43 p. text. [https://www.dnr.wa.gov/publications/ger_ms2018-05_geol_map_centralia_24k.zip]
- Sadowski, A. J.; Becerra, R. I.; Toth, C. H.; Polenz, Michael; Anderson, M. L.; Lau, T. R.; Nesbitt, E. A.; Tepper, J. H.; DuFrane, S. A., 2019, Geologic map of the Adna 7.5-minute quadrangle, Lewis County, Washington: Washington Geological Survey Map Series 2019-01, 1 sheet, scale 1:24,000. [https://www.dnr.wa.gov/publications/ger_ms2019-01_geol_map_adna_24k.zip]
- San Juan, Charles, 2022, Natural background groundwater arsenic concentrations in Washington State: Washington State Department of Ecology Publication No. 14-09-044, 72 p. [<https://apps.ecology.wa.gov/publications/documents/1409044.pdf>]
- Schasse, H. W., compiler, 1987, Geologic map of the Centralia quadrangle, Washington: Washington Division of Geology and Earth Resources Open File Report 87-11, 28 p., 1 plate, scale 1:100,000. [https://www.dnr.wa.gov/Publications/ger_ofr87-11_geol_map_centralia_100k.zip]
- Scott, K. M.; Vallance, J. W.; Pringle, P. T., 1995, Sedimentology, behavior, and hazards of debris flows at Mount Rainier, Washington: *U.S. Geological Survey Professional Paper* 1547, 56 p., 1 plate. [<https://pubs.er.usgs.gov/publication/pp1547>]
- Sherrod, B. L., 2001, Evidence for earthquake-induced subsidence about 1100 yr ago in coastal marshes of southern Puget Sound, Washington: *Geological Society of America Bulletin*, v. 113, no. 10, p. 1299–1311. [[https://doi.org/10.1130/0016-7606\(2001\)113%3C1299:EFEISA%3E2.0.CO;2](https://doi.org/10.1130/0016-7606(2001)113%3C1299:EFEISA%3E2.0.CO;2)]
- Sisson, T. W.; Vallance, J. W., 2009, Frequent eruptions of Mount Rainier over the last ~2,600 years: *Bulletin of Volcanology*, v. 71, no. 6, p. 595–618.
- Sisson, T. W.; Schmitt, A. K.; Danišik, Martin; Calvert, A. T.; Pempena, Napoleon; Huang, Chun-Yuan; Shen, Chuan-Chou, 2019, Age of the dacite of Sunset Amphitheater, a voluminous Pleistocene tephra from Mount Rainier (USA), and implications for Cascade glacial stratigraphy: *Journal of Volcanology and Geothermal Research*, v. 376, p. 27–43.
- Sláma, Jiří; Košler, Jan; Condon, D. J.; Crowley, J. L.; Gerdes, Axel; Hanchar, J. M.; Horstwood, M. S. A.; Morris, G. A.; Nasdala, Lutz; Norberg, Nicholas; Schaltegger, Urs; Schoene, Blair; Tubrett, M. N.; Whitehouse, M. J., 2008, Plešovice zircon—A new natural reference material for U-Pb and Hf isotopic microanalysis: *Chemical Geology*, v. 249, no. 1–2, p. 1–35. [<https://doi.org/10.1016/j.chemgeo.2007.11.005>]

- Snavely, P. D., Jr.; Roberts, A. E.; Hoover, Linn, Jr.; Pease, M. H., Jr., 1951, *Geology of the eastern part of the Centralia-Chehalis coal district, Lewis and Thurston Counties, Washington*: U.S. Geological Survey Coal Map 8, 2 sheets, scale 1:31,680. [https://pubs.er.usgs.gov/publication/coal8]
- Snavely, P. D., Jr.; Brown, R. D., Jr.; Roberts, A. E.; Rau, W. W.; Schopf, J. M., 1958, *Geology and coal resources of the Centralia-Chehalis district, Washington*: U.S. Geological Survey Bulletin 1053, 159 p., 6 plates. [https://doi.org/10.3133/b1053]
- Snavely, P. D., Jr.; Rau, W. W.; Hoover, Linn, Jr.; Roberts, A. E., 1959, McIntosh Formation, Centralia-Chehalis coal district, Washington. *In* Washington Division of Mines and Geology, Tertiary stratigraphic papers, southwestern Washington: Washington Division of Mines and Geology Reprint 3, 10 p. [https://www.dnr.wa.gov/publications/ger_reprint3_strat_papers_sw_wa.pdf]
- Steiger, R. H.; Jäger, Emilie, 1977, Subcommission on geochronology: Convention on the use of decay constant in geo- and cosmochronology: *Earth and Planetary Science Letters*, v. 36, p. 359–362. [https://doi.org/10.1016/0012-821X(77)90060-7]
- Sun, S.; McDonough, W. F., 1989, Chemical and isotopic systematics of oceanic basalts: implications for mantle composition and processes: Geological Society, London, Special Publications, v. 42, no. 1, p. 313–345. [https://doi.org/10.1144/GSL.SP.1989.042.01.19]
- Swick, C. A., 1942, Pendulum gravity measurements and isostatic reductions: U.S. Coast and Geodetic Survey Special Publication 232, 82 p.
- Tacoma-Pierce County Health Department, 2023, *Pierce County Water Quality* [webpage]: Tacoma-Pierce County Health Department. [accessed March 16, 2023, at https://piercecowa.maps.arcgis.com/apps/webappviewer/index.html?id=ea09ff7335974c20b89590db2586bf84]
- Telford, W. M.; Geldart, L. P.; Sheriff, R. E., 1990, *Applied geophysics*; 2nd ed.: Cambridge University Press, 770 p.
- Troost, K. G.; Booth, D. B., 2008, *Geology of Seattle and the Seattle area, Washington*. *In* Baum, R. L.; Godt, J. W.; Highland, L. M., editors, *Landslides and engineering geology of the Seattle, Washington, area*: Geological Society of America Reviews in Engineering Geology XX, p. 1–35. [https://doi.org/10.1130/2008.4020(01)]
- Troost, K. G., 2014, *Jokulhlaups from glacial Lake Puyallup, Pierce County, Washington: Ice Age Floods Institute Puget Lobe Chapter Field Trip September 20, 2014*, 38 p.
- Troost, K. G., 2016, *Chronology, lithology and paleoenvironmental interpretations of the penultimate ice-sheet advance into the Puget Lowland, Washington State*: University of Washington Doctor of Philosophy thesis, 239 p. [https://digital.lib.washington.edu/researchworks/handle/1773/38517]
- U.S. Geological Survey, 2016, SWWA foothills 2017 project, Western Washington 3DEP lidar, collected between Mar. 17 and Sept. 30, 2016 by Quantum Spatial Inc., 3-ft resolution, accessed April 16, 2023 [http://lidarportal.dnr.wa.gov/], metadata available on portal [https://lidarportal.dnr.wa.gov/download?ids=1079].
- U.S. Geological Survey Geologic Names Committee, 2018, Divisions of geologic time—Major chronostratigraphic and geochronologic units: U.S. Geological Survey Fact Sheet 2018-3054, 2 p. [https://pubs.usgs.gov/fs/2018/3054/fs20183054.pdf]
- Van Wagoner, T. M.; Crosson, R. S.; Creager, K. C.; Medema, G. F.; Preston, L. A.; Symons, N. P.; Brocher, T. M., 2002, Crustal structure and relocated earthquakes in the Puget Lowland, Washington, from high-resolution seismic tomography: *Journal of Geophysical Research Solid Earth*, v. 107, no. B12. [https://doi.org/10.1029/2001JB000710]
- Vallance, J. W.; Sisson, T. W., 2022, *Geologic field-trip guide to volcanism and its interaction with snow and ice at Mount Rainier, Washington*: U.S. Geological Survey Scientific Investigations Report 2017–5022–A, 76 p. [https://doi.org/10.3133/sir20175022A]
- Walker, J. D.; Geissman, J. W., compilers, 2009, *Geologic time scale*: Geological Society of America, 1 p. [https://www.geosociety.org/documents/gsa/timescale/timescl-2009.pdf]
- Walsh, T. J.; Korosec, M. A.; Phillips, W. M.; Logan, R. L.; Schasse, H. W., 1987, *Geologic map of Washington—Southwest quadrant: Washington Division of Geology and Earth Resources Geologic Map GM-34*, 2 sheets, scale 1:250,000, with 28 p. text. [http://www.dnr.wa.gov/publications/ger_gm34_geol_map_sw_wa_250k.pdf]
- Walsh, T. J.; Logan, R. L.; Polenz, Michael; Schasse, H. W., 2003a, *Geologic map of the Nisqually 7.5-minute quadrangle, Thurston and Pierce Counties, Washington*: Washington Division of Geology and Earth Resources Open File Report 2003-10, 1 sheet, scale 1:24,000. [https://www.dnr.wa.gov/publications/ger_ofr2003-10_geol_map_nisqually_24k.pdf]
- Walsh, T. J.; Polenz, Michael; Logan, R. L.; Lanphere, M. A.; Sisson, T. W., 2003b, Pleistocene tephrostratigraphy and paleogeography of southern Puget Sound near Olympia, Washington. *In* Swanson, Terry W., editor, *Western Cordillera and adjacent areas: Geological Society of America Field Guide 4*, p. 225–236.
- Walsh, T. J.; Logan, R. L., 2005, *Geologic map of the East Olympia 7.5-minute quadrangle, Thurston County, Washington*: Washington Division of Geology and Earth Resources Geologic Map GM-56, 1 sheet, scale 1:24,000. [http://www.dnr.wa.gov/Publications/ger_gm56_geol_map_eastolympia_24k.pdf]
- Walters, K. L., 1965, Mashel Formation of southwestern Pierce County, Washington. *In* Cohee, G. V.; West, W. S., *Changes in stratigraphic nomenclature by the U.S. Geological Survey, 1964*: U.S. Geological Survey Bulletin 1224-A, p. 55–59. [https://doi.org/10.3133/b1224A]
- Walters, K. L.; Kimmel, G. E., 1968, Ground-water occurrence and stratigraphy of unconsolidated deposits, central Pierce County, Washington: Washington Department of Water Resources Water Supply Bulletin 22, 428 p., 3 plates. [https://fortress.wa.gov/ecy/publications/SummaryPages/WSB22.html]
- Washington Department of Natural Resources, 2021, *Thurston 2021 project, Thurston County, Washington Lidar Technical Data Report*, collected between March 27 and April 3, 2021 by NV5 Geospatial Corvallis, 3-ft resolution, accessed April 16, 2023 [http://lidarportal.dnr.wa.gov/], metadata available on portal [https://lidarportal.dnr.wa.gov/download?ids=1517].
- Washington Geological Survey, 2019, *Oil and gas wells—GIS data: Washington Geological Survey Digital Data Series 21*, version 3.4, previously released July, 2016. [https://fortress.wa.gov/dnr/geologydata/publications/data_download/ger_portal_oil_gas.zip]
- Washington Geological Survey, 2023, *Geophysics Database—GIS data: Washington Geological Survey Digital Data Series 28*, version 1.0, April 2023. [https://fortress.wa.gov/dnr/geologydata/publications/data_download/ger_portal_geophysics.zip]
- Wells, R. E., 1990, Paleomagnetic rotations and the Cenozoic tectonics of the Cascade arc, Washington, Oregon, and California: *Journal of Geophysical Research Solid Earth*, v. 95, no. B12, p. 19,409–19,417. [https://doi.org/10.1029/JB095iB12p19409]
- Wells, R. E.; McCaffrey, Robert, 2013, Steady rotation of the Cascade arc: *Geology*, v. 41, no. 9, p. 1027–1030. [https://doi.org/10.1130/G34514.1]
- Wells, Ray; Bukry, David; Friedman, Richard; Pyle, Doug; Duncan, Robert; Haeussler, Peter; Wooden, Joe, 2014, *Geologic history of Siletzia, a large igneous province in the Oregon and Washington Coast Range: Correlation to the geomagnetic polarity time scale and implications for a long-lived Yellowstone hotspot*: *Geosphere*, v. 10, no. 4, p. 692–719. [https://doi.org/10.1130/GES01018.1]
- Wiedenbeck, Michael; Allé, P.; Corfu, Fernando; Griffin, W. L.; Meier, Martin; Oberli, Felix; Von Quadt, Albrecht; Roddick, J. C.; Spiegel, W., 1995, Three natural zircon standards for U-Th-Pb, Lu-Hf, trace element and REE analyses: *Geostandards Newsletters*, v. 19, p. 1–23. [https://doi.org/10.1111/j.1751-908X.1995.tb00147.x]

- Williams, I. S., 1997, U-Th-Pb geochronology by ion microprobe. *In* McKibben, M. A.; Shanks III, W. C.; Ridley, W. I., editors, Applications of microanalytical techniques to understanding mineralizing processes: Reviews in Economic Geology, v. 7, p. 1–35. [<https://doi.org/10.5382/Rev.07>]
- Wood, P. R., 1960, Geology and ground-water features of the Butte Valley region, Siskiyou County, California: U.S. Geological Survey Water Supply Paper 1491, 150 p. [<https://doi.org/10.3133/wsp1491>]

Appendix A. Geochronology

RADIOCARBON DATING

Overview

Carbon-14 (^{14}C) dating analyzes the radioactive decay of ^{14}C to ^{13}C . The half-life of ^{14}C is about 5,700 years. This makes the technique useful for dating carbon-containing material less than about 45,000 years old, and especially less than about 35,000 years old. We use ^{14}C dating on charcoal and other organic material within sedimentary units to help constrain their age of deposition.

Sample Collection and Preparation

We picked carbonaceous samples out of sedimentary exposures or drill core material and placed each sample in a zip-lock bag. As soon as practical, we either saturated or oven-dried the sample to prevent modern carbon growth. We further examined and cleaned the sample as needed to exclude modern organic growth (such as rootlets) that could contaminate the analysis with post-depositional carbon. We placed the final sample in a fresh zip-lock plastic bag, wrapping some small samples in aluminum foil inside the zip-lock bag to avoid static cling and light exposure inside the bag. We then mailed the sample to the lab for analysis.

Analytical Methods

Two different laboratories each analyzed a subset of our samples. Their respective procedures are separately outlined below.

BETA ANALYTIC

The following text is reproduced with little modification from the Beta Analytic website and describes their general procedure. A more-detailed white paper on their method can be found at www.radiocarbon.com/PDF/AMS-Methodology.pdf.

Before radiocarbon dating, the sample is first gently crushed then dispersed in deionized water. It is then washed with hot HCl acid to eliminate carbonates followed by an alkali wash (NaOH) to remove secondary organic acids. The alkali wash is followed by a final acid rinse to neutralize the solution before drying. Chemical concentrations, temperatures, exposure times, and number of repetitions depend on the sample submitted. Each chemical solution is neutralized prior to application of the next. During these serial rinses, mechanical contaminants such as associated sediments and rootlets are eliminated.

Treated samples are then analyzed by Accelerator Mass Spectrometry (AMS). The AMS measurement is done on graphite produced by hydrogen reduction of a CO_2 sample over a cobalt catalyst. The CO_2 is obtained from the combustion of the sample at $800^\circ\text{C}+$ under a 100 percent oxygen atmosphere. The CO_2 is first dried with methanol/dry ice then collected in liquid nitrogen for the subsequent graphitization reaction. The identical reaction is performed on reference standards, internal quality assurance samples, and backgrounds to ensure systematic chemistry.

The analytical result is obtained by measuring sample $^{14}\text{C}/^{13}\text{C}$ relative to the $^{14}\text{C}/^{13}\text{C}$ in Oxalic Acid II (NIST-4990C) in one of Beta Analytic's multiple in-house particle accelerators using SNICS ion source. Quality assurance (QA) samples are measured along with the unknowns and reported separately in a 'QA report'. The radiocarbon dating lab requires results for the QA samples to fall within expectations of the known values prior to accepting and reporting the results for any given sample.

The AMS result is corrected for total fractionation using machine graphite $\delta^{13}\text{C}$. The $\delta^{13}\text{C}$ reported for the sample is obtained by different ways depending upon the sample material. Solid organics are sub-sampled and converted to CO_2 with an elemental analyzer (EA). Water and carbonates are acidified in a gas bench to produce CO_2 . Both the EA and the gas bench are connected directly to an isotope-ratio mass spectrometer (IRMS). The IRMS performs the separation and measurement of the CO_2 masses (44, 45, and 46) and calculation of the sample $\delta^{13}\text{C}$.

Beta Analytic reports results in both uncalibrated and, if applicable, calibrated age statements. Beta Analytic believes that for samples older than 43,500 yr BP, the radioactivity of the material is statistically the same as the background. Samples that yield an activity at or below 43,500 yr BP are reported as "greater than" 43,500 yr BP.

DIRECT AMS

The following text is reproduced with little modification from the DirectAMS website at www.directams.com/process and describes their general procedure.

Samples are photographed and inspected for appropriateness of the requested services. Any discrepancies are discussed with the submitter. Samples then proceed through portioning/subsampling, physical and chemical pre-treatment protocols, production of CO_2 by combustion or acid digestion, reduction of CO_2 to graphite, preparation of graphite for measurement, measurement of carbon isotopes by Accelerator Mass Spectrometer (AMS), and data analysis, as appropriate for the type of sample. DirectAMS operates two different AMS instruments, an NEC Pelletron 500 kV and an IonPlus MICADAS 250 kV. Design differences between these instruments are detailed on the DirectAMS website; the general principle in the analysis is the same.

DirectAMS reports results in units of percent modern carbon (pMC) and the uncalibrated radiocarbon age before present (BP). All results have been corrected for isotopic fractionation with an unreported $\delta^{13}\text{C}$ value, measured on the prepared carbon by the AMS. The pMC reported requires no further correction for fractionation. After ~40,000 years, less than 1% of the original ^{14}C remains in a sample, reducing the precision of measurement. For DirectAMS, any measurement that falls below 0.369 pMC, exceeding 45,000 years old, is not distinguished from the measured level of background carbon.

Results

We collected and analyzed three charcoal samples from alluvium exposed along a channel cutbank on the west side of the Nisqually River (age sites GD1–GD3) and one wood sample from peat intersected by a sonic drill core beneath Vashon Drift (age site GD4) north of the Deschutes River. Summary age data are in Table 1, with more details in Table A1 below; laboratory reports are in the Data Supplement.

Table A1. Radiocarbon results from age sites GD1–GD4. See Data Supplement for laboratory reports.

Site ID	GD1	Maximum depositional age from charcoal fragment (below age site GD2) near base of pumiceous dark sand, 1.5 m below top of 4.5-m-high Nisqually River cutbank. Sampled 9/15/2022 by Rebecca Goughnour and Michael Polenz. Lab: DirectAMS. 2-sigma calibrated age (cal yr BP): 2,693–2,640 (10.9%) or 2,614–2,595 (4.7%) or 2,499–2,350 (79.8%), calibrated by M. Polenz using Oxcal online 11/22/2022.
Field sample ID	BHm031B3	
Map unit	Qvl	
TRS location	Sec. 19, T16N R03E	
Latitude (degrees)	46.8626406	
Longitude (degrees)	-122.4779369	
Elevation (ft)	375	
Age (^{14}C yr BP) $\pm 1\sigma$		2,414 ± 29
Site ID	GD2	Maximum depositional age from charcoal fragment near base of pumiceous pale sand (above age site GD1), 1.4 m below top of 4.5-m-high Nisqually River cutbank. Sampled 9/20/2022 by Michael Polenz and Trevor Contreras. Lab: DirectAMS. 2-sigma calibrated age (cal yr BP): 2,742–2,692 (34.9%) or 2,640–2,612 (16.1%) or 2,595–2,498 (44.4%), calibrated by M. Polenz using Oxcal online 11/22/2022.
Field sample ID	BHm031A2	
Map unit	Qvl	
TRS location	Sec. 19, T16N R03E	
Latitude (degrees)	46.8626406	
Longitude (degrees)	-122.4779369	
Elevation (ft)	375	
Age (^{14}C yr BP) $\pm 1\sigma$		2,535 ± 26
Site ID	GD3	Maximum depositional age from charcoal fragment from river level mud at base of Nisqually River cutbank, 4.5 m below relict terrace surface. Sampled 7/27/2022 by Michael Polenz and Trevor Contreras. Lab: DirectAMS. 2-sigma calibrated age (cal yr BP): 2,848–2,810 (20.0%) or 2,794–2,742 (75.5%), calibrated by M. Polenz using Oxcal online 11/22/2022.
Field sample ID	BHm031g	
Map unit	Qvl	
TRS location	Sec. 19, T16N R03E	
Latitude (degrees)	46.8626406	
Longitude (degrees)	-122.4779369	
Elevation (ft)	360	
Age (^{14}C yr BP) $\pm 1\sigma$		2,667 ± 27
Site ID	GD4	Radiocarbon infinite wood fragment from top of at least 2-m-thick peat intersected by sonic drill (courtesy of Weyerhaeuser Co.) between 35 m and at least 37 m below surface. Sampled 10/29/2021 by Michael Polenz. Lab: Beta Analytic.
Field sample ID	MLm197-115b	
Map unit	Qpu	
TRS location	Sec. 9, T15N R03E	
Latitude (degrees)	46.8041003	
Longitude (degrees)	-122.4298197	
Elevation (ft)	767	
Age (^{14}C yr BP) $\pm 1\sigma$		>43,500

U-Pb ZIRCON DATING

Overview

U-Pb dating uses radioactive decay of uranium (multiple isotopes) to lead (also multiple isotopes) to estimate the crystallization age of uranium-bearing minerals. We sample rocks or sediment to assess the crystallization ages of zircons within the deposit, and thereby estimate the igneous rock crystallization age, or constrain the maximum possible age of sediment deposition: meaning that the sediment deposit must be younger than the zircons within it. More than 100 zircons are usually analyzed from one sample of sediment or sedimentary rock; volcanic deposits may be analyzed with fewer zircons because most or all zircons are expected to be of similar age. Each zircon yields a separate, individual crystal age. Because zircons of different ages within a detrital sample can have different geologic (and geographic) sources, inferences on sedimentary provenance can also be made from zircon age spectra.

Sample Collection and Preparation

We generally collect about 2–10 kg of freshly exposed rock per sample, while avoiding contact with soil or other surface deposits that could introduce extraneous zircons; weathering and alteration do not usually affect the age of zircon and therefore pose no concern for this technique. We send our samples to ZirChron, LLC, for mineral separation using the following procedure:

Samples are pressure washed with water and then disaggregated using an Electro Pulse Disaggregator (EPD, Marx generator) at 1 Hz with discharges of ~250 kV for 15 minutes. Any clasts >500 μm are crushed in a crusher or pulverizer. Using stainless steel sieves, the fraction between 350 μm and 25 μm is retained and then processed using the Wilfley water table, Frantz paramagnetic separator, and a two-step (3.00 g/cm³ and 3.32 g/cm³) heavy liquid methylene iodide separation. Zircon grains from each sample are hand selected and mounted in epoxy, polished to expose the grain centers, and regions suitable for analysis are identified from optical imaging.

U-Pb Analytical Methods

The following text is reproduced from a technical write-up by the Washington State University Radiogenic Isotope and Geochronology Laboratory with minimal modification:

Zircon U-Pb ages are measured at the Radiogenic Isotope and Geochronology Lab (RIGL) at Washington State University using an Analyte G2 193 excimer laser ablation system coupled with a Thermo-Finnigan Element 2 single-collector inductively coupled plasma mass spectrometer. The laser parameters are 25- μm -diameter spot size, 10 Hz repetition rate, and fluence of ~5.0 J/cm². For the U-Pb measurement, we mostly followed the method of Chang and others (2006) and Gaschnig and others (2010), except for the use of a 193-nm laser system. A 10-second blank measurement of the He and Ar carrier gasses (laser off) before each analysis is followed by 250 scans across masses ²⁰²Hg, ²⁰⁴Pb+Hg, ²⁰⁶Pb, ²⁰⁷Pb, ²⁰⁸Pb, ²³²Th, ²³⁵U, and ²³⁸U during ~30-second laser ablation periods. Analyses of zircon unknowns, standards, and quality control zircon grains are interspersed with analyses of external calibration standards, typically with 10–12 unknowns bracketed by multiple analyses of two different zircon standards (Plešovice and FC-1). The Plešovice standard (337 Ma; Sláma and others, 2008) is used to calibrate the ²⁰⁶Pb/²³⁸U and ²⁰⁷Pb/²³⁵U ages, and the FC-1 standard (1,099 Ma; Paces and Miller, 1993) is used for calibration of ²⁰⁷Pb/²⁰⁶Pb ages owing to its high count rate for ²⁰⁷Pb (~2–4 times higher than that of Plešovice). Zircon 91500 (1,065 Ma; Wiedenbeck and others, 1995), Fish Canyon Tuff (~27.5 Ma; Lanphere and Baadsgaard, 2001) and Temora2 (417 Ma; Black and others, 2004) are used as quality control standards. Data are processed offline using the Iolite software (Paton and others, 2011). Common Pb correction is performed using the ²⁰⁷Pb method (Williams, 1997).

Results

We collected and analyzed eight samples (age sites GD6–GD13). GD6 is from unit **RMc**—sediment that resembles Mashel Formation and appears correlative with that unit's type section but yielded a Pliocene age that conflicts with the Miocene Mashel Formation definition. The other seven samples are Eocene Northcraft Formation or Eocene sedimentary rocks of unit **Ens**. Reported ages are as interpreted by Michael Polenz, who selected ages reported as age of the youngest single zircon from among the lab-reported age spectra (Data Supplement). Depositional ages from a coherent group of ages using the TuffZirc algorithm (Ludwig, 2003) were computed by the lab. Age interpretations are summarized in Table 1, where maximum constraining ages are reported as "<##", in contrast to the direct analytical results ["##"] shown in Table A2 below.

Table A2. $^{238}\text{U}/^{206}\text{Pb}$ ages of zircons from the Bald Hill 7.5-Minute quadrangle. See Data Supplement for full analytical results.

Site ID	GD6	Maximum depositional age from youngest of 76 detrital zircons from fluvial pumiceous sand and mud with leaf fossils from about 2 m above water level along the Nisqually River. Sampled 8/11/2022 by M. Polenz and Trevor Contreras.
Field sample ID	BHm016B	
Map unit	RMc	
TRS location	Sec. 26, T16N R03E	
Latitude (degrees)	46.84500	
Longitude (degrees)	-122.38742	
Elevation (ft)	436	
Age (Ma) $\pm 2\sigma$		4.1 ± 0.2

Site ID	GD7	Depositional age computed using TuffZirc from a coherent group of 47 zircon ages in a spectrum of 50 zircon ages from dacite tuff. Sampled 9/1/2022 by F. Hladky and M. Polenz.
Field sample ID	BHf048	
Map unit	Evt η	
TRS location	Sec. 11, T15N R03E	
Latitude (degrees)	46.7964504	
Longitude (degrees)	-122.3824171	
Elevation (ft)	1,494	
Age (Ma) $\pm 2\sigma$		38 ± 0.4

Site ID	GD8	Maximum depositional age from youngest of 120 detrital zircons from sandstone about 4 m above road and representing lowest exposed lithology at site. Sampled 10/26/2022 by A. Steely, J. Tepper, and M. Polenz.
Field sample ID	BHm188	
Map unit	Ens	
TRS location	Sec. 16, T15N R03E	
Latitude (degrees)	46.7854258	
Longitude (degrees)	-122.4416184	
Elevation (ft)	800	
Age (Ma) $\pm 2\sigma$		39.2 ± 0.4

Site ID	GD9	Crystallization age computed using TuffZirc from a coherent group of 38 zircon ages in a spectrum of 43 zircon ages from dacite. Sampled 9/15/2022 by F. Hladky and M. Polenz.
Field sample ID	BHf066	
Map unit	Evd η	
TRS location	Sec. 19, T15N R03E	
Latitude (degrees)	46.775031	
Longitude (degrees)	-122.475397	
Elevation (ft)	1,105	
Age (Ma) $\pm 2\sigma$		40.5 ± 0.5

Site ID	GD10	Maximum depositional $^{238}\text{U}/^{206}\text{Pb}$ age from youngest of 60 detrital zircons from a debris flow deposit that mostly consists of andesite tuff breccia but also entrained fragments of the marine sediment separately analyzed by GD11. Sampled 8/23/2022 by F. Hladky, M. Polenz, and E. and M. Nesbitt
Field sample ID	BHm038A	
Map unit	Evcn	
TRS location	Sec. 22, T15N R03E	
Latitude (degrees)	46.767806	
Longitude (degrees)	-122.409736	
Elevation (ft)	1,165–1,190	
Age (Ma) $\pm 2\sigma$		39.2 ± 0.7

Site ID	GD11	Maximum depositional $^{238}\text{U}/^{206}\text{Pb}$ age from youngest of 110 detrital zircons from marine sediment with shallow-subtidal marine fossils. Sampled 8/23/2022 by F. Hladky, M. Polenz, and E. and M. Nesbitt.
Field sample ID	BHm038b	
Map unit	Ens	
TRS location	Sec. 22, T15N R03E	
Latitude (degrees)	46.7675349	
Longitude (degrees)	-122.4096930	
Elevation (ft)	1,160	
Age (Ma) $\pm 2\sigma$		48 ± 0.4

Site ID	GD12	Crystallization age computed using TuffZirc from a coherent group of 34 zircon ages in a spectrum of 55 zircon ages from diorite. Sampled 9/13/2022 by F. Hladky and M. Polenz.
Field sample ID	BHm082b	
Map unit	Eid η	
TRS location	Sec. 26, T15N R03E	
Latitude (degrees)	46.755797	
Longitude (degrees)	-122.382622	
Elevation (ft)	1,415	
Age (Ma) $\pm 2\sigma$		36.5 ± 0.4

Site ID	GD13	Maximum depositional $^{238}\text{U}/^{206}\text{Pb}$ age from youngest of 96 detrital zircons from planar-bedded, micaceous sandstone and siltstone. Sampled 09/14/2022 by M. Polenz and F. Hladky.
Field sample ID	BHm098b	
Map unit	Ens	
TRS location	Sec. 25, T15N R02E	
Latitude (degrees)	46.7502327	
Longitude (degrees)	-122.4893729	
Elevation (ft)	1,915	
Age (Ma) $\pm 2\sigma$		35.2 ± 1.2

$^{40}\text{Ar}/^{39}\text{Ar}$ ARGON DATING

Overview

Argon dating uses the radioactive decay of ^{40}K to ^{40}Ar to determine the age of potassium-bearing minerals and materials. We use argon dating to estimate the crystallization ages of the groundmass or selected crystal fractions (such as plagioclase) in igneous rocks.

Sample Collection and Preparation

Samples for argon dating are collected from in-place volcanic or volcanoclastic rock and should have as little weathering and alteration as possible. We prioritize relatively unweathered rock with few fractures, though such exposures are not abundant in the map area. Blocks of the outcrop are broken into smaller pieces to remove weathering rinds. We then place about 1–3 kg of rock into a bag. Candidate sample sites are ranked based on many factors, including the desire for spatial coverage, stratigraphic location, rock type, and budgetary constraints. Of those samples that will be analyzed, we select the freshest pieces and send 1–2 kg of material to the lab for irradiation and analysis.

Analytical Methods

The following section of text is reproduced from an analytical report provided by the Oregon State University Argon Geochronology Laboratory, with minimal modification:

Samples were crushed, sieved, washed, and dried using standard mineral separation techniques. Groundmass splits were obtained for the sample, rinsed with cold water, then dried in a drying oven at 55 °C. Once the samples were dried, they were sieved to 250–150 µm. Special care was taken to remove any alteration material by using an intensive acid leaching procedure using a combination of HCl and HNO₃ at different acid strength (Koppers and others, 2000). A final separate of groundmass was obtained using a binocular microscope. Any visible alteration or adhering crystal phases were carefully removed prior to packaging and irradiation of the sample.

$^{40}\text{Ar}/^{39}\text{Ar}$ ages were obtained by incremental heating methods using the ThermoFisher Scientific ARGUS-VI mass spectrometer and data collection using internal lab software ArArExperiments version 4.4.0. The samples were irradiated for 6 hours. Samples were irradiated with the Fish Canyon Tuff sanidine (FCT-2-NM sanidine) with an age of 28.201 ± 0.023 Ma, 1σ flux monitor (Kuiper and others, 2008). Individual J-values for each sample were calculated by polynomial extrapolation of the measured flux gradient against irradiation height and typically give 0.06–0.12 percent uncertainties (1σ). The $^{40}\text{Ar}/^{39}\text{Ar}$ incremental heating age determinations were performed on a multi-collector ARGUS-VI mass spectrometer at Oregon State University that has five Faraday collectors fitted to two 1,012 ohm resistors for masses ^{41}Ar and ^{40}Ar and three 1,013 ohm resistors for argon masses ^{39}Ar , ^{38}Ar , and ^{37}Ar and one ion-counting CuBe electron multiplier (located in a position next to the lowest mass Faraday collector). This allows us to measure simultaneously all argon isotopes, with mass 36 on the multiplier and masses 37 through 40 on the four adjacent Faradays. This configuration provides the advantages of running in a full multi-collector mode while measuring the lowest peak (on mass 36) on the highly sensitive electron multiplier (which has an extremely low dark-noise and a very high peak/noise ratio). Irradiated samples were loaded into Cu-planchettes in an ultra-high vacuum sample chamber and incrementally heated by scanning a Synrad Firestar 20-watt defocused CO₂ laser beam in pre-set patterns across the sample, in order to release the argon evenly. Each heating step is 62 seconds. After heating, reactive gasses were cleaned up using four SAES Zr-Al API0 getters for 3 minutes; two operated at 450 °C and two operated at room temperature (21 °C). All ages were calculated using the corrected Steiger and Jäger (1977) decay constant of $5.530 \pm 0.097 \times 10^{-10} \text{ yr}^{-1}$ (2σ) as reported by Min and others (2000). For all other constants used in the age calculations we refer to table 2 in Koppers and others (2003). Incremental heating plateau ages and isochron ages were calculated as weighted means with $1/\sigma^2$ as weighting factor and as YORK2 least-square fits with correlated errors using the ArArCALC v2.7.0 (Beta Version) software from Koppers (2002), available online at <http://earthref.org/ArArCALC/>.

Argon isotopic results are corrected for system blanks, radioactive decay, mass discrimination, reactor-induced interference reactions, and atmospheric argon contamination. Decay constants reported by Min and others (2000) are utilized for age calculation. Isotope interference corrections as determined using the ARGUS VI are: ($^{36}\text{Ar}/^{37}\text{Ar}$)Ca = 0.0002703 ± 0.000005; ($^{39}\text{Ar}/^{37}\text{Ar}$)Ca = 0.0006425 ± 0.0000059; ($^{40}\text{Ar}/^{39}\text{Ar}$)K = 0.000607 ± 0.000059; ($^{38}\text{Ar}/^{39}\text{Ar}$)K = 0.012077 ± 0.000011. Ages were calculated assuming an atmospheric $^{40}\text{Ar}/^{36}\text{Ar}$ ratio of 298.56 ± 0.113 (Lee and others, 2006). Data reduction and age calculation were processed using ArArCALC 2.7.0 (Koppers, 2002). Plateau ages are defined as including >50% of the total ^{39}Ar released with at least three consecutive steps, where the $^{40}\text{Ar}/^{39}\text{Ar}$ ratio for each step is in agreement with the mean at the 95% confidence level. In many cases only a mini-plateau age is given, where a mini-plateau contains <50% of the ^{39}Ar released.

Results

We analyzed four Northcraft Formation samples (age sites GD14–GD17). Among the four samples, both groundmass and plagioclase were analyzed in two, only groundmass in one, and only plagioclase in the fourth, for a total of six analyses. Reported errors are internal only, meaning that they exclude sources of errors external to the sample preparation and lab analysis such as unrecognized sample characteristics or flawed interpretive assumptions. Summary data are in Table 1, with more details in Table A1 below; laboratory reports are in the Data Supplement.

Table A3. New $^{40}\text{Ar}/^{39}\text{Ar}$ ages from the Bald Hill 7.5-minute quadrangle. Where both groundmass and plagioclase phases were analyzed, the age we prefer is **bold**. MSWD is the mean squared weighted deviation, also known as the reduced chi-squared statistic.

Site ID	GD14	Age (Ma) ±2σ	Age type	Material	% total ³⁹ Ar included in age	Heating steps included in age	MSWD
Field sample ID	BHf033	37.40 ±0.08	mini-plateau	groundmass	49.19	6	2.05
Lab ID	23F01486	Age dates eruption of black, glassy columnar basaltic andesite from quarry along Weyerhaeuser Truck Road SE 800 m east of Bass Lake (north of Bald Hill). Sampled 8/24/2022 by F. Hladky.					
Geochemical classification	Basaltic andesite						
Map unit	Evaη						
TRS location	Sec. 35, T16N R03E						
Latitude (degrees)	46.83012						
Longitude (degrees)	-122.39844						
Elevation (ft)	664						

Site ID	GD15	Age (Ma) $\pm 2\sigma$	Age type	Material	% total ^{39}Ar included in age	Heating steps included in age	MSWD
Field sample ID	BHm084	37.81 \pm 0.08	plateau	plagioclase	66.69	17	1.60
Lab ID	23F01632	<p>Age dates plagioclase crystallization in lithic pumiceous dacite ash flow tuff east of Green Hill containing hornblende crystals, angular dacite blocks, and subrounded pumice blocks.</p> <p>Sampled 9/13/2022 by F. Hladky and M. Polenz.</p>					
Geochemical classification	dacite						
Map unit	Evt η						
TRS location	Sec. 14, T15N R03E						
Latitude (degrees)	46.79127						
Longitude (degrees)	-122.40118						
Elevation (ft)	1,133						

[illegible]

Appendix B. Geochemistry

OVERVIEW

We use major- and trace-element analyses to classify igneous rocks in the map area and aid in their identification and correlation. Our 44 samples span a range of rock types and are dispersed throughout Eocene to Pliocene time.

SAMPLE COLLECTION AND PREPARATION

We select samples for geochemical analysis from intrusive, volcanic, and volcanoclastic rocks. We use hammers, usually a small sledge hammer, to break off the freshest pieces. Where we are concerned about possible contamination from hammer streaks, we try to remove those, usually by using fragments of the same sample to scrape or break off any streaks. We generally submit between ~100 and ~200 g of the freshest available material for lab analysis, except where sample sizes are necessarily smaller, for example, among smaller pumice clasts.

ANALYTICAL METHODS

We reproduce the following abbreviated methods directly from documents provided by the ALS Geochemistry Laboratory in Vancouver, British Columbia; only general descriptions of methods are provided by ALS on their website:

Major-element percentages are determined on a fused bead after acid digestion using Inductively Coupled Plasma-Atomic Emission Spectroscopy (ICP-AES) (ALS analysis code ME_ICP06). A prepared sample (0.1 g) is added to lithium metaborate/lithium tetraborate flux, mixed well, and fused in a furnace at 1,025 °C. The resulting melt is then cooled and dissolved in an acid mixture containing nitric, hydrochloric, and hydrofluoric acids. This solution is then analyzed by ICP-AES. Results are corrected for spectral inter-element interferences.

Loss on Ignition (LOI) (ALS analysis code OA_GRA05) is determined using a 1 g sample, placed in an oven at 1,000 °C for one hour, cooled, and then weighed again. The percent loss on ignition is calculated from the difference in weight before and after ignition.

Trace element concentrations are determined using Inductively Coupled Plasma-Mass Spectroscopy (ICP-MS) (ALS analysis code ME_MS81). Samples are prepared following the same lithium borate fusion and digestion procedure as applied in ICP-AES analyses, but are subjected to an additional lithium borate fusion and an acid digestion procedure prior to analysis on the ICP-MS.

RESULTS

We obtained results for 44 samples. Sample locations are shown on the Map Sheet (geochemistry sites G#s); analytical data are in the Data Supplement.

Appendix C. Geophysics

GRAVITY

Overview and Purpose

Lateral changes in isostatic gravity across a region result from density changes within rocks of the mid-to-upper crust. Gridding gravity measurements creates a map that outlines areas of high gravity and low gravity. Areas of high gravity indicate that high-density rocks (for example, many igneous and metamorphic rocks) are closer to the surface. Areas of low gravity indicate that less-dense material is near the surface, such as sediment within a basin. Gravity surveys are especially useful in delineating steeply dipping contacts between two rock bodies that have a large contrast in density. Gravity data, combined with measured rock densities, allow us to quantitatively test models of subsurface geology against our observations.

Description of Method

FIELD METHODS AND SAMPLED LOCATIONS

Measurements from 347 new gravity stations were collected using a Scintrex CG-6 meter (Serial # 19050174) and combined with measurements from Finn and others (1991), PACES (now defunct; data obtained from B. Drenth, U. S. Geological Survey, written commun., 2020), Polenz and others (2021, 2022), and WGS unpublished data (2021). We utilize base station ‘OLYK’ with ties to Chehalis B (Nilsen, 1976) and Johnston Ridge Observatory (Washington Geological Survey, 2023) to tie our data to the U.S. gravity network.

Gravity station spacing at roughly 2 km generates a basic grid over a large area. Where known structures exist or initial gravity data collection showed a significant gradient, station spacing is reduced to 1 km to provide greater resolution. Forty nine new bedrock density samples and 316 magnetic susceptibility measurements collected from exposed bedrock help to constrain our geophysical models.

DATA REDUCTION AND PROCESSING

A Javad Triumph-2 differential GPS unit provided the horizontal and vertical position of each station. Proprietary Javad Justin software allows us to carefully edit data and post-process for differential correction using the National Oceanic and Atmospheric Administration and the National Geodetic Survey’s Continuously Operating Reference Stations (CORS) within 70 km of the study area. After processing, typical positional accuracy is 0.15 m in the vertical and horizontal. Suspect GPS elevations were replaced with lidar data where those appear to be good. We apply the gravimeter’s factory calibration constants to each gravity observation, augmented by correction factors obtained from the Mount Hamilton calibration loop east of San Jose, CA (Barnes and others, 1969), and correcting for Earth tides to produce observed gravity values. The data reference the International Gravity Standardization Net of 1971 (Morelli, 1974) and the reference ellipsoid is the Geodetic Reference System of 1967 (International Union of Geodesy and Geophysics, 1971). The assumed linear drift between base-station ties results in a maximum gravity reading error of 0.05 mGal.

Gravity data reduction formulas for the free-air anomaly are standard (for example, Telford and others, 1990; Swick, 1942) and we applied Bouguer, Earth curvature, and terrain corrections out to 166.7 km from each station to produce a complete Bouguer anomaly. Terrain corrections incorporate a field-based component (to a radius of 68 m using the Hayford system; Plouff, 2000). The complete Bouguer anomaly is further reduced to an isostatic anomaly using an Airy-Heiskanen model (Heiskanen and Vening-Meinesz, 1958) that produces the isostatic correction, assuming a 25-km-thick crust at sea level and a crust-mantle density contrast of 400 kg/m³. All parts of the data reduction process assume a standard reduction density of 2,670 kg/m³. Average uncertainty in steep and hilly regions is 0.12–0.23 mGal, whereas average uncertainty in flatter areas is 0.05–0.1 mGal.

We use the minimum-curvature algorithms in the GIS software package Geosoft Oasis Montaj to transform our point isostatic anomaly data into gridded surfaces. The maximum horizontal gradients (referred to as “max-spots”) calculated using the curvature analysis methodology of Phillips and others (2007) quantitatively locate strong and linear boundaries between rocks in the subsurface that have substantial density differences.

HAND SAMPLE DENSITIES

We collected bedrock samples throughout the study area for laboratory analysis. We weighed samples using an A & D company limited FX-3000i WP analytical balance. We combined three measurements per sample to determine density: a dry weight in air, a submerged (water-saturated) weight, and a water-saturated weight in air. We used the saturated bulk density in our modeling as it best reflects subsurface conditions.

GEOMAGNETICS

Overview and Purpose

Magnetic surveys map local changes in the Earth's magnetic field due to local magnetic sources at high resolution. This method delineates contacts between geologic units of contrasting magnetic properties, particularly in the mid- to upper crust. Collecting a large number of magnetic profiles helps to precisely determine magnetic contacts and trace them across a map area. Individual profiles, coupled with magnetic susceptibility measurements of surficial rocks, are powerful geophysical constraints for two-dimensional subsurface modeling.

Description of Method

Aeromagnetic data used in this study were acquired in 1995 and 2016 (Blakely and others, 1999, 2020) via low-flying aircraft with a stinger-mounted magnetometer. For the 1995 survey, north–south flight lines were spaced 0.4 km apart with east–west tie lines spaced at 8 km. For the 2016 survey, east–west flight lines were spaced 0.4 km apart with north–south tie lines spaced at 4 km. Aeromagnetic measurements were interpolated to a projected, rectilinear grid using a bi-directional gridding algorithm within the GIS software package Geosoft Oasis Montaj. We use a ‘reduced-to-pole’ filter to correct inclination and declination (such that Inc. = 0 deg, and Dec. = 0 deg). This correction centers anomalies over their sources for more precise map-view interpretation.

Hand-Sample Properties

In addition to the rock density measurements described above (see Gravity), we measured magnetic susceptibility of some hand samples. Magnetic susceptibility measurements taken with a KT10 Kappa Meter accompany rock sample density measurements, and we used the same meter to collect direct readings from outcrops where possible. Weathering tends to replace denser minerals with less dense weathering products and turn magnetite into less magnetic minerals like hematite. Therefore, all of our measured rock densities and susceptibilities from surface outcrops (see Data Supplement) can be considered minimum values.

QUANTITATIVE CROSS-SECTION MODELING

Overview and Purpose

Quantitative two-dimensional forward modeling of cross sections constrained by potential-field data provides insight into the geometry of units and structures geometry that go beyond qualitative interpretations of map-view data. This technique helps provide the best possible interpretations of structure types (for example normal, reverse, or strike-slip faults), fault or contact dips in the upper crust (for example steep or shallow), and offset across faults on units with particularly strong physical-property contrasts with surrounding rocks. This method also can identify blind faults that have little surface expression and are difficult to capture via surface geology observations.

Description of Method

GM-SYS provides a platform for computing the sum effect on both the gravitational and geomagnetic fields of the Earth from a given two-dimensional cross section of the subsurface. This is a forward-modeling method, meaning that the operator hypothesizes which rock types are in the subsurface along with their location and geometry, and the GM-SYS program predicts the total fields that result from that particular model. The operator's responsibility is to refine the hypothesis until the predicted potential-fields match the data measured in the field. This ensures that any cross-section interpretation of the subsurface matches the potential field data and the field-observed surface geology.

Several types of data constrain this process in addition to the gravity and aeromagnetic data. Surface geology constrains the model's near-surface geometry, while laboratory measurements of density and magnetic properties of hand samples gathered from the surface (see above) and at depth from the E.F.E. Willhoite et al. No. 1 gas well (Washington Geological Survey, 2019; Contreras and others, 2023) provide additional rock property constraints. Also essential is the knowledge of the operator and collaborators in the project about the geologic history, expected stratigraphy in the subsurface, and structural geometries that are physically possible based on standard geologic mapping and cross-section construction techniques.

There is still a possibility that multiple hypotheses of subsurface geometry can fit the gravity and magnetic data within the accepted error for those two data types. Therefore, care in the construction of models, and testing various hypothesis, can help define which parts of the subsurface model are well constrained.

In general, potential-field data provide strong constraints on the position and dip of simple, steeply-dipping boundaries between rocks with strong differences in physical properties. However, potential-field data provide very poor constraints on horizontal boundaries or boundaries between rocks with little contrast in physical properties. Depth of sub-horizontal stratigraphic boundaries within sedimentary rocks is particularly suspect and is never well-constrained without the addition of good quality well or reflection-seismic data. Depth of sub-horizontal boundaries between units of strongly contrasting properties is resolvable

depending on uncertainties in the physical properties of those units. Where geophysical properties are uncertain, the depth of a boundary trades off with density and/or magnetism of the juxtaposed rocks.

In our modeling approach, we first construct an initial simplified model, including uniform packages of sediment, sedimentary rock, metamorphic rock, and volcanic rock that fit the long-wavelength features in the gravity and magnetic data. Our model space extends beyond the end of the models shown in this report to avoid edge effects due to truncated subsurface volumes. We iteratively add detail in the stratigraphy and decrease the size of blocks, particularly near the surface, to fit shorter wavelength anomalies. During each iteration, we test possible options for rock properties and geometries of boundaries that are possible given the surface geology observations and measured rock-property constraints. Once repeated iterations provide a similar solution to fit the data, then we conclude that we have converged on a model with a good fit to the data.

Appendix D. Landsat Spectral Image Analysis

OVERVIEW AND PURPOSE

We analyzed multispectral satellite images to add insights where field data were sparse, or to help us identify areas for additional field work. Our multispectral analysis uses pixel responses at multiple electromagnetic wavelengths to obtain information about the materials within each pixel. We use our field observations to identify multispectral signatures that correlate to particular rock or sediment types and then use these to identify areas where the spectral data suggest otherwise unrecognized types of rocks or sediment for which we may want to seek additional field observations, or to infer surface lithologic information and help identify map units and (or) locate geologic map unit boundaries where field data are sparse.

DESCRIPTION OF METHOD

We combined:

1. 30-m-resolution multispectral imagery from the U.S. Geological Survey-operated Operational Land Imager (OLI) mounted to the Landsat 8 (NASA) satellite.
2. 100-m-resolution Thermal Infrared Sensor (TIRS) imagery, also from the Landsat 8 (NASA) satellite.
3. A 30-m-resolution digital elevation model (DEM) from the Japanese Advanced Spaceborne Thermal Emission and Reflection Radiometer (ASTER) remote sensing instrument mounted to the NASA-launched Terra satellite.

Landsat 8 provides geospatial imagery in 11 bands of data ranging from ultra blue (0.435–0.451 μm wavelengths) to Thermal 2 (11.50–12.51 μm wavelengths). We used Landsat 8 OLI images (all bands except Band 8) and TIRS images, collected in 2015. We combined the Landsat images with DEM data, which Brown and others (2007) found improves separability between “classes” (meaning, lithologic categories identified by our analysis of the geospatial image data). We used ASTER 30 m DEM data (version 2) because, like the Landsat 8 image data, it comes in 30 m resolution, which simplifies our image processing. We used ENVI 5.3 image analysis software to visualize, process, and analyze this geospatial imagery, including post-processing for atmospheric correction (to clean up the diffusion and scattering of light in the spectral images), and image enhancement as described by Ali and others (2012).

In a process referred to as supervised classification we used spectral signatures from 1:100,000-scale geologic mapping (Schasse, 1987) to define groupings (classes) of spectral signatures (meaning, hypothesized that similar spectral signatures elsewhere also correspond to similar geologic materials or concealing surface cover), such as bedrock, basalt, peat, sand, clay, and water—as described, for instance, by Kettles and others (2000). We did this using the Maximum Likelihood classification algorithm in ENVI, which calculates the probability that a given pixel belongs to a specific class by assuming that the statistics for each class in each band are normally distributed. We then used locations where we had field observations (training sites) to iteratively refine matches between spectral signatures and classes by redefining classes where needed, and by progressively subdividing classes that yielded varied spectral signatures and therefore lacked distinction relative to other categories, as described by Brown and others (2007). We processed the classified data into both images and polygons to provide flexibility in displaying the results. The images are visually messier but more nuanced and the polygons allow more display options, for instance by displaying only selected classes.

RESULTS

In our densely vegetated western Washington map area, the geospatial classification data are no substitute for field mapping and should not be over-interpreted—as also suggested by analyses of less vegetated areas (for instance, Kettles and others, 2000; Brown and others, 2007). We used them to help target some of our field data collection and to inform poorly constrained calls where field data are sparse.